

NASA Technical Memorandum 104540

IN-33
52267
P-97

Numerical and Experimental Study of Curved and Planar Frequency Selective Surfaces with Arbitrary Illumination

Armen Caroglanian

April 1991

(NASA-TM-104540) NUMERICAL AND EXPERIMENTAL
STUDY OF CURVED AND PLANAR FREQUENCY
SELECTIVE SURFACES WITH ARBITRARY
ILLUMINATION M.S. Thesis - Maryland Univ.,
1989 (NASA) 97 p

N92-12185

CSCD 09C G3/33

Unclas
0052267

NASA



NASA Technical Memorandum 104540

**Numerical and Experimental
Study of Curved and Planar
Frequency Selective Surfaces
with Arbitrary Illumination**

Armen Caroglanian
Goddard Space Flight Center
Greenbelt, Maryland



National Aeronautics and
Space Administration

Goddard Space Flight Center
Greenbelt, MD

1991

INTELLIGENCE BOARD

ABSTRACT

Title of Thesis: NUMERICAL AND EXPERIMENTAL STUDY
 OF CURVED AND PLANAR FREQUENCY
 SELECTIVE SURFACES WITH ARBITRARY
 ILLUMINATION

Name of degree candidate: Armen Caroglanian

Degree and Year: Master of Science, 1989

Thesis directed by: Dr. Kevin J. Webb
 Assistant Professor
 Electrical Engineering Department

A frequency selective surface (FSS) composed of apertures in a metallic sheet is known as an inductive FSS. The infinite inductive FSS theory is derived and the aperture fields are solved by a spectral domain formulation with method of moments solution. Both full domain and subsectional basis functions are studied. A locally planar technique (LPT) is used to determine the forward scattered field from a generally shaped inductive FSS with arbitrary illumination.

An experimental FSS study describing test methods and results is presented to verify both the infinite FSS theory and determine the accuracy of the LPT. The infinite planar FSS transmission coefficient measured as a function of frequency is compared with theory. The inductive FSS's forward scattered field is experimentally measured and compared to the LPT. A series of experiments with the spherical feed source at varying distances from the planar FSS is used to determine the limitations of the LPT in terms of the incident phase error over a unit cell. The limitations of the LPT due to surface curvature is investigated by an experimental study of the scattered fields from a set of

hyperbolic cylinders of different curvatures. From the experiments, guidelines for applying the LPT are developed.

TABLE OF CONTENTS

CHAPTER 1. INTRODUCTION	1
CHAPTER 2. INFINITE INDUCTIVE FSS ANALYSIS	
2.1 Introduction	5
2.2 Spectral Domain Formulation	5
2.3 Spectral Moment Method	14
2.4 Basis Functions	20
2.5 Transmission Coefficient	27
CHAPTER 3. LOCALLY PLANAR TECHNIQUE (LPT)	
3.1 Introduction	31
3.2 Region I. Feed Source	33
3.3 Region II. Inductive FSS	35
3.4 Region III. Forward Scattered Fields	35
3.5 Locally Planar Technique Summary	38
CHAPTER 4. FREQUENCY RESPONSE OF THE INDUCTIVE FSS: NUMERICAL AND EXPERIMENTAL RESULTS	
4.1 Inductive FSS Design	39
4.2 Transmission Coefficient Magnitude: Numerical and Experimental Results	42

4.3 Transmission Coefficient Phase:	
Numerical and Experimental Results	49
CHAPTER 5. INDUCTIVE FSS FORWARD SCATTERED FIELD	
EXPERIMENTS AND MODELING	
5.1 Introduction	53
5.2 Scattered Field Experiments With Plane Wave Incidence	
on a Planar FSS	56
5.3 Study of the LPT Accuracy as a Function of Incident	
Field Curvature	65
5.4 Study of the LPT Accuracy as a Function of Surface	
Curvature	78
CHAPTER 6. CONCLUSIONS	86
REFERENCES	89

ACKNOWLEDGEMENTS

The author would like to thank his thesis advisor, Dr. Kevin J. Webb, for his guidance and advice in the FSS study. A very special thanks goes to Billy B. Williams of the RF Systems Section for the countless hours of effort in performing the numerous FSS experiments. The author also thanks Preston W. Grounds and Richard F. Schmidt for their helpful explanations and clarifications of the FSS theory.

SECRET

CHAPTER 1

INTRODUCTION

The frequency selective surface (FSS) is a useful filter for electromagnetic radiation ranging from microwave to optical frequencies [1]. Two types of FSSs exist. The capacitive type, illustrated in Fig. 1.1, is composed of metallic patches on a dielectric substrate. The inductive type, shown in Fig. 1.2, consists of apertures in a metallic sheet. The dots in both figures signify that the patches and apertures are a part of an infinite FSS. The response of the infinite planar inductive FSS is determined from a spectral moment method solution derived in Chapter 2. A typical capacitive and inductive FSS response about the resonant frequency, f_0 , is shown on the right side of Figs. 1.1 and 1.2. Note the magnitude of the reflection coefficient in the capacitive case is equivalent to the magnitude of the transmission coefficient for the inductive case. This is valid if the patches and apertures can be interchanged to transform the one type of FSS to the other. The duality of the frequency responses can be explained by Babinet's principle [2].

In many FSS applications, such as radomes and subreflectors, the FSS is curved and has non-planar illumination. Figure 1.3 is an example of a reflector antenna utilizing a hyperbolic FSS to separate the S-band Cassegrain feed and K-band prime feed [3]. The FSS shape is a hyperboloid of revolution and the incident wave is spherical. The general analysis of curved FSSs is an extremely difficult problem. An approximate method, called the locally planar technique, (LPT) can be used to predict the response from a planar or curved FSS with arbitrary illumination. This technique has been applied to the case of a parabolic cylinder FSS by Ko and Mittra [4]. This technique, presented in Chapter 3, breaks the FSS into a number of subarrays each of which is assumed to be a segment of an infinite planar surface. The infinite

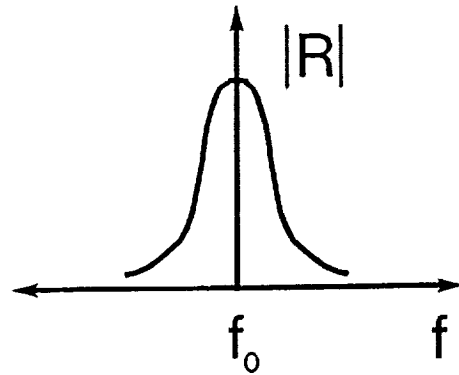
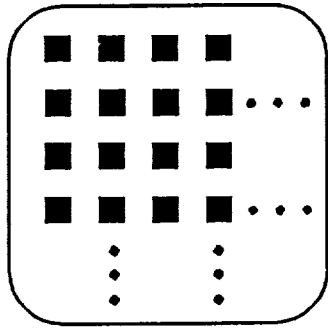


Figure 1.1. Capacitive FSS metallic patch geometry and the magnitude of the reflection coefficient as a function of frequency.

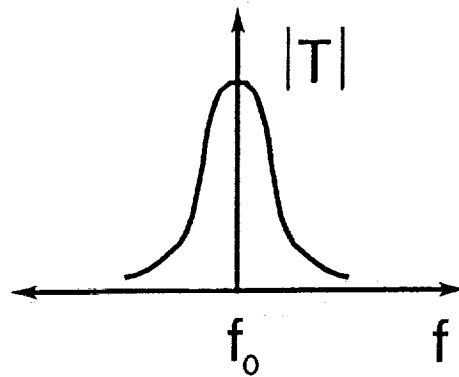
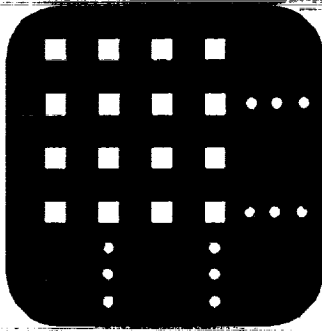


Figure 1.2. Inductive FSS apertures in a metallic sheet and the magnitude of the transmission coefficient as a function of frequency.

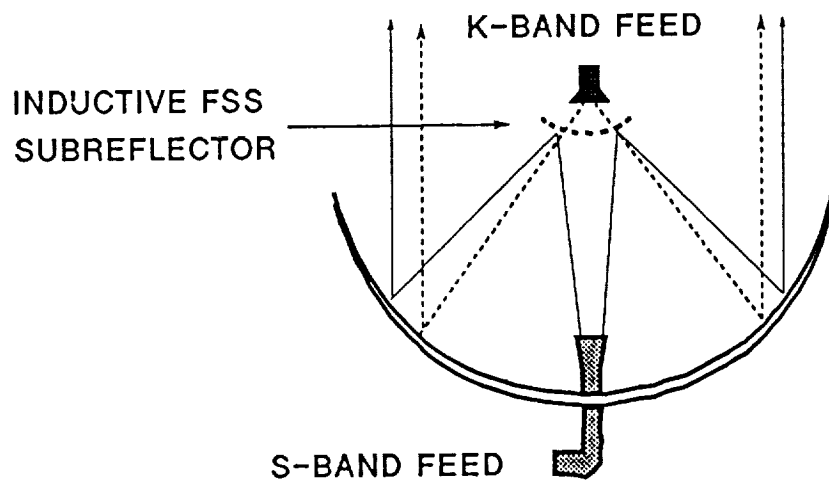


Figure 1.3. Dual reflector antenna system with an inductive FSS subreflector separating the prime and Cassegrain feeds.

FSS theory is applied to each subarray and the total response is found from a superposition of individual responses.

However, there are limitations for the FSS geometries which can be solved by the LPT. At some value of incidence phase front curvature and or surface curvature, the LPT is no longer valid. In the literature, the limitations of the LPT for predicting the scattered fields from the general FSS problem has not been addressed. Thus, a major goal of the FSS study was to determine the regions of validity for the LPT theory. To study the LPT as well as verify the infinite planar FSS analysis, an inductive FSS was designed and fabricated. An extensive experimental FSS study was undertaken at the NASA / Goddard Space Flight Center. Chapter 4 describes the infinite planar experimental techniques and results from the transmission coefficient measurements as a function of frequency. In Chapter 5 two types of LPT experiments and scattered field pattern results are presented. The first LPT experiment is for a planar FSS with varying incident field curvature. The second LPT experiment is for a set of hyperbolic cylinders of varying curvature with near planar illumination. By comparing theory and experiment, guidelines for applying the LPT are developed. From the guidelines, a given FSS problem can be evaluated for its suitability for LPT analysis.

CHAPTER 2

INFINITE INDUCTIVE FSS ANALYSIS

2.1 Introduction

The infinite inductive and capacitive FSS has been analyzed by a number of authors over the years [4]-[8]. The spectral domain moment method technique applied to the inductive FSS in this chapter is based primarily on the work of Tsao and Mittra [8]. A good summary of the technique is given in the text titled *The Spectral Domain in Electromagnetics* [9]. The FSS theory presented here is for an infinitesimally thin FSS illuminated by a plane wave. The analysis begins from basic electromagnetic theory. From a spectral domain method of moments solution, the unknown aperture fields are calculated.

2.2 Spectral Domain Formulation

The analysis begins by considering the inductive FSS illustrated in Fig. 2.1. The FSS is composed of rectangular apertures placed in a rectangular grid arrangement. A unit cell of the FSS is defined as the region enclosed by the dashed line in Fig. 2.1. The dimensions of the unit cell are equal to the aperture-to-aperture spacing in each direction. Figure 2.2 illustrates the incident plane wave geometry. The incident electric and magnetic fields are given by \mathbf{E}^{inc} and \mathbf{H}^{inc} . The plane wave's propagation vector, \mathbf{k}^{inc} , is oriented at an angle θ from the z -axis and at an angle ϕ from the x -axis. The analysis assumes the FSS to have zero thickness. The experimental FSS had a thickness much less than the smallest wavelength of interest, so the assumption of zero thickness is valid in the theory. The scattered magnetic field from an aperture, \mathbf{H}^s , is derived from the electric vector potential \mathbf{F}

$$\mathbf{H}^s = -j\omega\epsilon\mathbf{F} + \frac{1}{j\omega\mu}\nabla(\nabla\cdot\mathbf{F}). \quad (2.1)$$

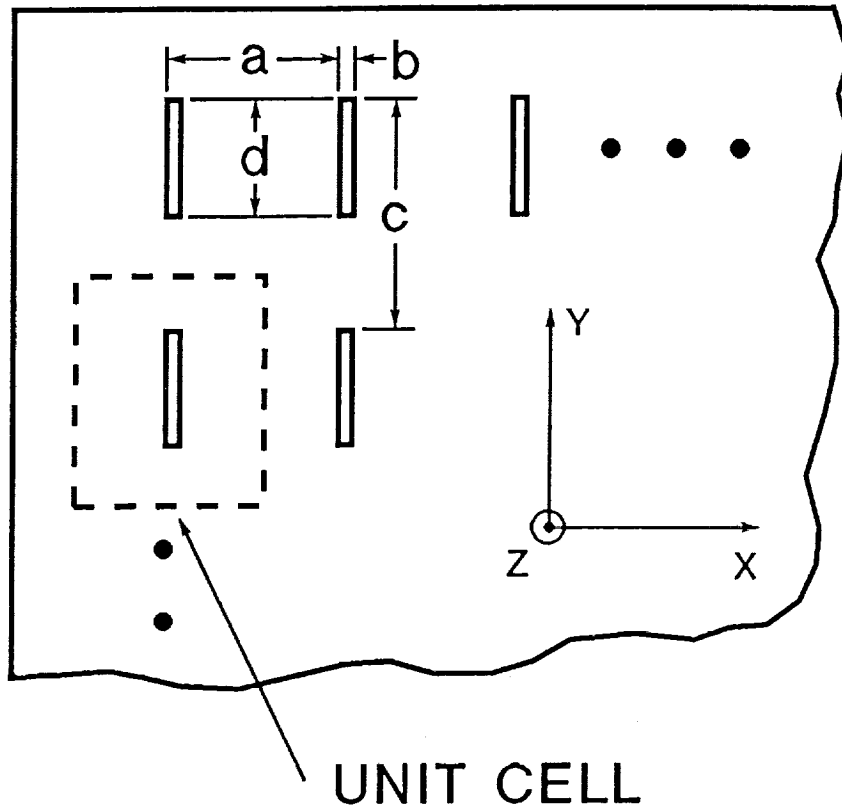


Figure 2.1. Inductive FSS aperture geometry. The FSS shown is a small portion of the larger "infinite" FSS.

The electric vector potential, \mathbf{F} , is found from the magnetic current \mathbf{K} . \mathbf{K} in turn is derived from the equivalence principle for electric fields [10]. The equivalent magnetic current is placed above a perfect electric conductor (PEC) and has the value

$$\mathbf{K} = \mathbf{E} \times \mathbf{n}. \quad (2.2)$$

The orientation of the unit vector \mathbf{n} is normal to the FSS in the direction of the half space in which the fields are desired. The electric vector potential \mathbf{F} in the (x, y) plane, based on the definition $\mathbf{E} = -\nabla \times \mathbf{F}$, is derived from \mathbf{K} and the Green's function G by

$$\mathbf{F}(x, y) = \begin{pmatrix} F_x \\ F_y \end{pmatrix} = \begin{pmatrix} G * K_x \\ G * K_y \end{pmatrix}. \quad (2.3)$$

The symbol $*$ is the convolution operator. K_x and K_y are the components of \mathbf{K} in the \mathbf{a}_x and \mathbf{a}_y directions respectively. The Green's function G is defined by

$$G(x, y) = \frac{e^{-jk_0 r}}{4\pi r}. \quad (2.4)$$

In the (x, y) plane,

$$r = \sqrt{x^2 + y^2}. \quad (2.5)$$

The free space propagation constant is

$$k_0 = \frac{2\pi}{\lambda} = \frac{2\pi f}{c}. \quad (2.6)$$

The frequency of operation is f , and c is the speed of light. Using the identity dyadic $\overline{\overline{I}}$, $\overline{\overline{G}}$ is defined as

$$\bar{\bar{G}} = G\bar{I} = G \begin{pmatrix} 1 & 0 \\ 0 & 1 \end{pmatrix}. \quad (2.7)$$

Equation (2.3), for the electric vector potential, can be written as

$$\mathbf{F}(x, y) = \bar{\bar{G}} * \mathbf{K}. \quad (2.8)$$

Returning to (2.1) for the scattered magnetic field and expanding in the Cartesian coordinate frame yields

$$\begin{aligned} \mathbf{H}^s(x, y) = & -j\omega\epsilon(F_x\mathbf{a}_x + F_y\mathbf{a}_y) + \\ & \frac{1}{j\omega\mu} \left[\frac{\partial}{\partial x} \left(\frac{\partial F_x}{\partial x} + \frac{\partial F_y}{\partial y} \right) \mathbf{a}_x + \frac{\partial}{\partial y} \left(\frac{\partial F_x}{\partial x} + \frac{\partial F_y}{\partial y} \right) \mathbf{a}_y \right]. \end{aligned} \quad (2.9)$$

Equation (2.9) can be written into matrix format and simplified by pulling out the $1/j\omega\mu$ term and noting $k_0^2 = \omega_0^2\mu\epsilon$. The scattered magnetic field in the (x, y) plane is

$$\mathbf{H}^s(x, y) = \frac{1}{j\omega\mu} \begin{pmatrix} \frac{\partial^2}{\partial x^2} + k_0^2 & \frac{\partial}{\partial x} \frac{\partial}{\partial y} \\ \frac{\partial}{\partial x} \frac{\partial}{\partial y} & \frac{\partial^2}{\partial y^2} + k_0^2 \end{pmatrix} \mathbf{F}(x, y). \quad (2.10)$$

\mathbf{H}^s is transformed into the spectral domain by the Fourier transform defined by

$$\tilde{\mathbf{H}}^s(\alpha, \beta) = \int_{-\infty}^{\infty} \int_{-\infty}^{\infty} \mathbf{H}^s(x, y) e^{-j(\alpha x + \beta y)} dx dy, \quad (2.11)$$

where $\tilde{\mathbf{H}}^s$ denotes the transform of \mathbf{H}^s . The spectral variables α and β take on discrete values, the phase constant values for the Floquet modes, which for the rectangular cell are [11]

$$\alpha_m = \frac{2\pi m}{a} + k_x^{inc} \quad m = 0, \pm 1, \pm 2, \dots \quad (2.12a)$$

$$\beta_n = \frac{2\pi n}{c} + k_y^{inc} \quad n = 0, \pm 1, \pm 2, \dots \quad (2.12b)$$

k_x^{inc} and k_y^{inc} are the projections of the incident propagation vector into the (x, y) plane. The constants a and c are the unit cell dimensions in the x and y directions respectively. From Fig. 2.2,

$$k_x^{inc} = k_0 \sin \theta \cos \phi \quad (2.13a)$$

$$k_y^{inc} = k_0 \sin \theta \sin \phi. \quad (2.13b)$$

The equations derived in the spatial domain are transformed into the spectral domain by means of the following equivalent operators:

$$\mathbf{A}(x, y) * \mathbf{B}(x, y) \implies \tilde{\mathbf{A}}(\alpha, \beta) \tilde{\mathbf{B}}(\alpha, \beta) \quad (2.14a)$$

$$\frac{\partial}{\partial x} \mathbf{A}(x, y) \implies j\alpha \tilde{\mathbf{A}}(\alpha, \beta) \quad (2.14b)$$

$$\frac{\partial}{\partial y} \mathbf{A}(x, y) \implies j\beta \tilde{\mathbf{A}}(\alpha, \beta). \quad (2.14c)$$

The transform of the scattered magnetic field, \mathbf{H}^s , is found by applying (2.14b) and (2.14c) to (2.10). The result is

$$\tilde{\mathbf{H}}_s(\alpha, \beta) = \frac{1}{j\omega\mu} \begin{pmatrix} k_0^2 - \alpha^2 & -\alpha\beta \\ -\alpha\beta & k_0^2 - \beta^2 \end{pmatrix} \tilde{\mathbf{F}}(\alpha, \beta). \quad (2.15)$$

Applying relation (2.14a) to the electric vector potential equation (2.8) results in

$$\tilde{\mathbf{F}}(\alpha, \beta) = \tilde{\tilde{G}}\tilde{\mathbf{K}} \quad (2.16)$$

The Fourier transform of the Green's function, is [12]

$$\tilde{G}(\alpha, \beta) = \frac{-j}{2\sqrt{k_0^2 - \alpha^2 - \beta^2}} \quad k_0^2 > (\alpha^2 + \beta^2) \quad (2.17a)$$

for the propagating modes, and

$$\tilde{G}(\alpha, \beta) = \frac{1}{2\sqrt{\alpha^2 + \beta^2 - k_0^2}} \quad k_0^2 < (\alpha^2 + \beta^2) \quad (2.17b)$$

for the evanescent modes. Substituting (2.16) into (2.15) yields

$$\tilde{\mathbf{H}}^s = \frac{1}{j\omega\mu} \begin{pmatrix} k_0^2 - \alpha^2 & -\alpha\beta \\ -\alpha\beta & k_0^2 - \beta^2 \end{pmatrix} \tilde{\tilde{G}}\tilde{\mathbf{K}}. \quad (2.18)$$

The scattered magnetic field in the spatial domain, \mathbf{H}^s , is found by taking the inverse Fourier transform, giving

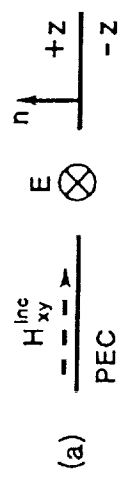
$$\mathbf{H}^s = \frac{1}{4\pi^2} \int_{-\infty}^{\infty} \int_{-\infty}^{\infty} \tilde{\mathbf{H}}^s(\alpha, \beta) e^{j(\alpha x + \beta y)} d\alpha d\beta. \quad (2.19)$$

The integral becomes a summation since the magnetic current, $\tilde{\mathbf{K}}$, is non-zero at discrete points only. \mathbf{H}^s in the spatial domain is

$$\mathbf{H}^s = \frac{1}{4\pi^2 j\omega\mu} \sum_{m=-\infty}^{\infty} \sum_{n=-\infty}^{\infty} \begin{pmatrix} k_0^2 - \alpha^2 & -\alpha\beta \\ -\alpha\beta & k_0^2 - \beta^2 \end{pmatrix} \tilde{\tilde{G}}\tilde{\mathbf{K}} e^{j(\alpha x + \beta y)}. \quad (2.20)$$

To uniquely determine the magnetic currents in the aperture, the boundary conditions at the $z = 0$ plane will be evaluated. Figure 2.3(a) illustrates

INCIDENT REGION
EQUIVALENT PROBLEM



TRANSMISSION REGION
EQUIVALENT PROBLEM

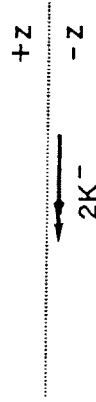
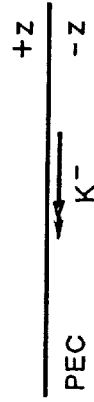
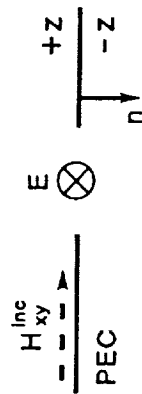


Figure 2.3. Equivalence and method of images formulation.

(a) original problem.

(b) Equivalent magnetic field representation.

(c) Method of images fields and currents in free space.

the original problem with the aperture field \mathbf{E} and the incident magnetic field in the plane of the FSS, \mathbf{H}_{xy}^{inc} . Figure 2.3(b). illustrates the equivalent magnetic current backed by a PEC for both incident and transmission regions. In the incident region, the equivalent magnetic current \mathbf{K} and magnetic field \mathbf{H}_{xy}^{inc} are located an infinitesimal distance ϵ above the PEC. From the method of images, when the PEC is removed, equivalent fields and currents can be determined for the free space region illustrated in Fig. 2.3(c). The resulting magnetic field and magnetic current have doubled.

The magnetic field in the (x, y) plane due to the magnetic current \mathbf{K} is given by \mathbf{H}^s . The total magnetic field, \mathbf{H}^+ , in the incident region at $z = +\epsilon$, is

$$\mathbf{H}^+ = 2\mathbf{H}_{xy}^{inc} + 2\mathbf{H}^s. \quad (2.21)$$

In the transmission region, for the continuity of the tangential electric field, the magnetic current $\mathbf{K}^- = -\mathbf{K}^+$. The magnetic field in the transmission region, at $z = -\epsilon$, shown in Fig. 2.2c, is due entirely to $2\mathbf{K}$ and given by

$$\mathbf{H}^- = -2\mathbf{H}^s. \quad (2.22)$$

The aperture field is continuous, so as $\epsilon \rightarrow 0$

$$\mathbf{H}^- = \mathbf{H}^+. \quad (2.23)$$

Equating (2.21) and (2.23) and simplifying yields the relation between the incident and scattered field on the (x, y) plane

$$\mathbf{H}^s = \frac{\mathbf{H}_{xy}^{inc}(x, y)}{2}. \quad (2.24)$$

Substituting the above into (2.20), replacing $\tilde{\mathbf{K}}^+$ with $\tilde{\mathbf{E}} \times \mathbf{a}_z$, and simplifying yields

$$\mathbf{H}_{xy}^{inc} = \frac{j}{\omega\mu 2\pi^2} \sum_{m=-\infty}^{\infty} \sum_{n=-\infty}^{\infty} \begin{pmatrix} \alpha\beta & k_0^2 - \alpha^2 \\ \beta^2 - k_0^2 & -\alpha\beta \end{pmatrix} \tilde{G} \tilde{\mathbf{E}} e^{j(\alpha x + \beta y)}, \quad (2.25)$$

the inductive FSS equation. In the next section, a solution technique will be presented to solve for the aperture electric fields.

2.3 Spectral Moment Method

In this section, the basis function weights will be found by the moment method implemented in the spectral domain. The inductive FSS equation (2.25), relating the unknown aperture field to the known incident field has the form

$$\mathbf{L}(\tilde{\mathbf{f}}) = \mathbf{g}. \quad (2.26)$$

\mathbf{L} is given by

$$\mathbf{L} = \frac{j}{\omega\mu 2\pi^2} \sum_{m=-\infty}^{\infty} \sum_{n=-\infty}^{\infty} \begin{pmatrix} \alpha\beta & k_0^2 - \alpha^2 \\ \beta^2 - k_0^2 & -\alpha\beta \end{pmatrix} \tilde{G} e^{j(\alpha x + \beta y)}. \quad (2.27)$$

The unknown \mathbf{f} is defined as

$$\mathbf{f} = \begin{pmatrix} E_x \\ E_y \end{pmatrix}, \quad (2.28)$$

where

$$E_x = \sum_{n=1}^{N_x} c_{x_n} E_{x_n}, \quad (2.29a)$$

$$E_y = \sum_{n=1}^{N_y} c_{y_n} E_{y_n}. \quad (2.29b)$$

E_{x_n} and E_{y_n} are the basis functions described in Section 2.4.

In (2.26) \mathbf{g} is given by

$$\mathbf{g} = \begin{pmatrix} H_x^{inc} \\ H_y^{inc} \end{pmatrix}. \quad (2.30)$$

The unknown complex constants, c_n , are determined by constructing a set of $N = N_x + N_y$ linearly independent equations. The equation set is formed by an inner product defined by

$$\langle \mathbf{A}, \mathbf{B} \rangle = \int \int_{aper} (\mathbf{A} \times \mathbf{B}^*) \cdot \mathbf{a}_z \, ds, \quad (2.31)$$

where the symbol $*$ denotes the complex conjugate. The inner product is taken on both sides of equation (2.26) with respect to the testing functions \mathbf{b}_n

$$\sum_{n=1}^N \langle \mathbf{L}(\tilde{\mathbf{f}}), \mathbf{b}_n \rangle = \langle \mathbf{g}, \mathbf{b}_n \rangle. \quad (2.32)$$

In the Galerkin's method, the testing functions are chosen to equal the basis functions [13], so

$$\mathbf{b}_n \in \{E_{x_n} \mathbf{a}_x, E_{y_n} \mathbf{a}_y\} \quad (2.33)$$

Equation (2.32) is composed of an x -component and y -component given by:

$$\frac{j}{\omega \mu 2\pi^2} \sum_{m=-\infty}^{\infty} \sum_{n=-\infty}^{\infty} \tilde{G}(\alpha\beta \tilde{E}_x + (k_0^2 - \alpha^2) \tilde{E}_y) e^{j(\alpha x + \beta y)} = H_x^{inc}, \quad (2.34a)$$

$$\frac{j}{\omega \mu 2\pi^2} \sum_{m=-\infty}^{\infty} \sum_{n=-\infty}^{\infty} \tilde{G}((\beta^2 - k_0^2) \tilde{E}_x - \alpha\beta \tilde{E}_y) e^{j(\alpha x + \beta y)} = H_y^{inc}, \quad (2.34b)$$

where \tilde{E}_x and \tilde{E}_y are the Fourier transforms of the aperture electric field in the \mathbf{a}_x and \mathbf{a}_y directions, respectively. To form a compact set of equations, the following substitutions will be made:

$$q_1 = \frac{j\tilde{G}}{\omega\mu 2\pi^2} (\alpha\beta) \quad (2.35a)$$

$$q_2 = \frac{j\tilde{G}}{\omega\mu 2\pi^2} (k_0^2 - \alpha^2) \quad (2.35b)$$

$$q_3 = \frac{j\tilde{G}}{\omega\mu 2\pi^2} (\beta^2 - k_0^2). \quad (2.35c)$$

The N simultaneous equations are formed by computing the inner products between (2.34) and the testing functions. Inner products are taken between the \mathbf{E}_x testing functions and (2.34b) and between the \mathbf{E}_y testing functions and (2.34a). This is a direct consequence of the cross product in the inner product definition. The form of the inner product on the left-hand side, $\langle LHS \rangle_x$, using (2.34b) for the x -directed testing function is

$$\langle LHS \rangle_x = \left\langle \sum_{m=-\infty}^{\infty} \sum_{n=-\infty}^{\infty} (q_3 \tilde{E}_x - q_1 \tilde{E}_y) e^{j(\alpha x + \beta y)} \mathbf{a}_y, E_{x_n} \mathbf{a}_x \right\rangle \quad (2.36a)$$

$$= (\mathbf{a}_y \times \mathbf{a}_x) \cdot \mathbf{a}_x \int \int_{aper} \sum_{m=-\infty}^{\infty} \sum_{n=-\infty}^{\infty} (q_3 \tilde{E}_x - q_1 \tilde{E}_y) E_{x_n}^* e^{j(\alpha x + \beta y)} dx dy. \quad (2.36b)$$

The integral can be written as a Fourier transform, of $\mathbf{E}_{x_n}^*$. The inner product in (2.36) becomes

$$\langle LHS \rangle_x = - \sum_{m=-\infty}^{\infty} \sum_{n=-\infty}^{\infty} (q_3 \tilde{E}_x - q_1 \tilde{E}_y) \tilde{E}_{x_n}^*. \quad (2.37a)$$

A similar result for the \mathbf{E}_y testing functions is

$$\langle LHS \rangle_y = \sum_{m=-\infty}^{\infty} \sum_{n=-\infty}^{\infty} (q_1 \tilde{E}_x + q_2 \tilde{E}_y) \tilde{E}_{y_n}^*. \quad (2.37b)$$

The y -component of the incident magnetic field on the (x, y) plane is given by

$$\mathbf{H}_y^{inc} = H_y^{inc} e^{j(\alpha(0)x + \beta(0)y)} \mathbf{a}_y. \quad (2.38)$$

The inner product on the right side for the x -directed testing function can be written as the zeroth spectral component of a Fourier transform

$$\langle RHS \rangle_x = \langle \mathbf{H}_y^{inc}, \mathbf{E}_{x_n} \rangle = -H_y^{inc} \tilde{E}_{x_n}^*(\alpha(0), \beta(0)). \quad (2.39)$$

The similar result for the y -directed testing functions is

$$\langle RHS \rangle_y = H_x^{inc} \tilde{E}_{y_n}^*(\alpha(0), \beta(0)). \quad (2.40)$$

The final set of equations for the inductive FSS is

$$\begin{aligned} \sum_{m=-\infty}^{\infty} \sum_{n=-\infty}^{\infty} (q_1 \tilde{E}_x + q_2 \tilde{E}_y) \tilde{E}_{y_1}^* &= H_x^{inc} \tilde{E}_{y_1}^*(\alpha(0), \beta(0)) \\ &\vdots \\ \sum_{m=-\infty}^{\infty} \sum_{n=-\infty}^{\infty} (q_1 \tilde{E}_x + q_2 \tilde{E}_y) \tilde{E}_{y_{N_y}}^* &= H_x^{inc} \tilde{E}_{y_{N_y}}^*(\alpha(0), \beta(0)) \\ \sum_{m=-\infty}^{\infty} \sum_{n=-\infty}^{\infty} (q_3 \tilde{E}_x - q_1 \tilde{E}_y) \tilde{E}_{x_1}^* &= H_y^{inc} \tilde{E}_{x_1}^*(\alpha(0), \beta(0)) \\ &\vdots \\ \sum_{m=-\infty}^{\infty} \sum_{n=-\infty}^{\infty} (q_3 \tilde{E}_x - q_1 \tilde{E}_y) \tilde{E}_{x_{N_x}}^* &= H_y^{inc} \tilde{E}_{x_{N_x}}^*(\alpha(0), \beta(0)) \end{aligned} \quad (2.41)$$

Substituting in the basis function expansion for the electric field (2.29) and writing in matrix form yields an equation of the form

$$[A][C] = [B]. \quad (2.42)$$

The matrix $[A]$ is given in Fig. 2.4. For computer implementation, the inner product summations are taken over a finite m and n set. The number of basis functions and spectral terms for a satisfactory convergent solution will be discussed in Chapter 4. The vector $[B]$ is

$$[B] = \begin{pmatrix} H_x^{inc} \tilde{E}_{y_1}^* (\alpha(0)\beta(0)) \\ \vdots \\ H_x^{inc} \tilde{E}_{y_{N_y}}^* (\alpha(0)\beta(0)) \\ \vdots \\ H_y^{inc} \tilde{E}_{x_1}^* (\alpha(0)\beta(0)) \\ \vdots \\ H_y^{inc} \tilde{E}_{x_{N_x}}^* (\alpha(0)\beta(0)) \end{pmatrix}. \quad (2.43)$$

Vector $[C]$ is the unknown weighting constants for the aperture field

$$[C] = \begin{pmatrix} c_{x_1} \\ \vdots \\ c_{x_{N_x}} \\ c_{y_1} \\ \vdots \\ c_{y_{N_y}} \end{pmatrix}. \quad (2.44)$$

The unknown $[C]$ in (2.42) is solved for by a numerical technique which is equivalent to

$$[C] = [A]^{-1}[B]. \quad (2.45)$$

The aperture fields are found by a superposition of the weighted basis functions defined in equation (2.29). The aperture field will be used in Section 2.5 to determine the amplitude and phase of the transmission coefficient. In Chapter 3, the forward scattered field from a finite FSS will be found from the transforms of the aperture fields.

$$\begin{bmatrix}
 \sum_m \sum_n q_1 \tilde{E}_{x_1} \tilde{E}_{y_1}^* & \dots & \sum_m \sum_n q_1 \tilde{E}_{x_{N_x}} \tilde{E}_{y_1}^* & \dots & \sum_m \sum_n q_2 \tilde{E}_{y_1} \tilde{E}_{y_1}^* & \dots & \sum_m \sum_n q_2 \tilde{E}_{y_{N_y}} \tilde{E}_{y_1}^* \\
 \vdots & & \vdots & & \vdots & & \vdots \\
 \sum_m \sum_n q_1 \tilde{E}_{x_1} \tilde{E}_{y_{N_y}}^* & \dots & \sum_m \sum_n q_1 \tilde{E}_{x_{N_x}} \tilde{E}_{y_{N_y}}^* & \dots & \sum_m \sum_n q_2 \tilde{E}_{y_1} \tilde{E}_{y_{N_y}}^* & \dots & \sum_m \sum_n q_2 \tilde{E}_{y_{N_y}} \tilde{E}_{y_{N_y}}^* \\
 \sum_m \sum_n q_3 \tilde{E}_{x_1} \tilde{E}_{x_1}^* & \dots & \sum_m \sum_n q_3 \tilde{E}_{x_{N_x}} \tilde{E}_{x_1}^* & \dots & - \sum_m \sum_n q_1 \tilde{E}_{y_1} \tilde{E}_{x_1}^* & \dots & - \sum_m \sum_n q_1 \tilde{E}_{y_{N_y}} \tilde{E}_{x_1}^* \\
 \vdots & & \vdots & & \vdots & & \vdots \\
 \sum_m \sum_n q_3 \tilde{E}_{x_1} \tilde{E}_{x_{N_x}}^* & \dots & \sum_m \sum_n q_3 \tilde{E}_{x_{N_x}} \tilde{E}_{x_{N_x}}^* & \dots & - \sum_m \sum_n q_1 \tilde{E}_{y_1} \tilde{E}_{x_{N_x}}^* & \dots & - \sum_m \sum_n q_1 \tilde{E}_{y_{N_y}} \tilde{E}_{x_{N_x}}^*
 \end{bmatrix}$$

Figure 2.4. Matrix [A].

2.4 Basis Functions

Two types of basis functions, the full domain and subsectional, are studied. The desired basis function set is one which can model the aperture fields with the least number of unknown weights, c_n . The basis functions ideally suited for the problem of basic geometrical aperture shapes are the full domain basis functions where apriori knowledge of the edge condition can be included. The experimental FSS described in Chapter 4 has rectangular apertures ideally suited for this type of basis function. The full domain basis functions have the property that each basis function spans the entire aperture. The subsectional basis functions, on the other hand, define each basis function over a different area of the FSS. The subsectional basis functions are useful for modeling the aperture fields for general aperture shapes. However, the subsectional method requires a large number of basis functions to model the fields accurately. Hence, the CPU time is much greater than for the full domain approach. In this section, both basis sets will be defined over a rectangular aperture and the Fourier transforms will be calculated. The basis functions are derived for the x -directed electric field only since the y -directed basis set is similar.

Full Domain Basis Functions

The basis functions used to model the x -component of the aperture electric fields in a rectangular aperture of dimension $b \times d$ are [14]

$$E_{x_n}(x, y) = \frac{T_p\left(\frac{2x}{b}\right)}{\left(1 - \left(\frac{2x}{b}\right)^2\right)^{\frac{1}{2}}} \sin\left(\frac{q\pi}{d}\left(y + \frac{d}{2}\right)\right), \quad (2.47a)$$

where

$$p = 0, 1, 2, \dots \quad \text{and} \quad q = 1, 2, \dots \quad (2.47b)$$

$T_p(x)$ is the Chebyshev function of order p . The first few Chebyshev functions

are given by [15]

$$\begin{aligned} T_0(x) &= 1 \\ T_1(x) &= x \\ T_2(x) &= 2x^2 - 1. \end{aligned} \tag{2.48}$$

Figure 2.5 shows the shape of the major full domain basis functions. The result of the Meixner edge condition is seen at $x = \pm \frac{b}{2}$.

The Fourier transform, (2.11), of the basis function is found by separating the functions into x and y components and transforming each into the spectral domain. In the space domain let

$$\mathbf{E}_{x_n} = f_x(x)f_y(y) \mathbf{a}_z. \tag{2.49}$$

The function f_x is defined by

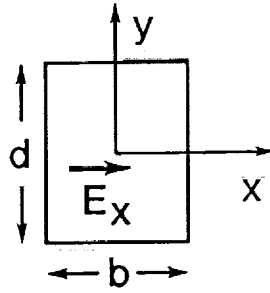
$$f_x(x) = P_b(x) \frac{T_p\left(\frac{2x}{b}\right)}{\left(1 - \left(\frac{2x}{b}\right)^2\right)^{\frac{1}{2}}}. \tag{2.50}$$

$P_b(x)$ is the unit pulse of width b centered at the origin. The transform of f_x is

$$\tilde{f}_x = \int_{-\infty}^{\infty} P_b(x) T_p\left(\frac{2x}{b}\right) \left(1 - \left(\frac{2x}{b}\right)^2\right)^{-\frac{1}{2}} e^{-j\alpha x} dx. \tag{2.51}$$

Making the change of variables $x_1 = \frac{2x}{b}$ and noting the integral is limited by the pulse yields

$$\tilde{f}_x = \frac{b}{2} \int_{-1}^1 T_p(x_1) (1 - (x_1)^2)^{-\frac{1}{2}} e^{-j(\alpha b x_1/2)} dx_1. \tag{2.52}$$



n	p	q	f_x	f_y
1	0	1		
2	0	2		
3	1	1		
4	1	2		

Figure 2.5. Full domain basis functions for modeling the E_x aperture electric field.

The integral is solved by associating terms with the known integral [16]

$$\int_{-1}^1 T_n(t)(1-t^2)^{-\frac{1}{2}} e^{-j\omega t} dt = (-1)^n (j)^n \pi J_n(\omega), \quad (2.53)$$

where $J_n(\omega)$ is the Bessel function of the first kind of order n . The transform \tilde{f}_x becomes

$$\tilde{f}_x = \frac{b}{2} (-1)^p (j)^p \pi J_p\left(\frac{\alpha b}{2}\right). \quad (2.54)$$

The y -dependent term is

$$f_y = P_d(y) \sin\left(\frac{q\pi}{d}\left(y + \frac{d}{2}\right)\right). \quad (2.55)$$

The transform is taken by separately transforming the sine and pulse functions and convolving the two functions in the spectral domain. The Fourier transforms needed are

$$\begin{aligned} P_d(y) &\Rightarrow d \operatorname{sinc}\left(\frac{\beta d}{2}\right) \\ \sin\left(\frac{q\pi}{d}\left(y + \frac{d}{2}\right)\right) &\Rightarrow -j\pi \left[\delta\left(\beta - \frac{q\pi}{d}\right) - \delta\left(\beta + \frac{q\pi}{d}\right) \right] e^{j\beta d/2} \\ f_1(y)f_2(y) &\Rightarrow \frac{1}{2\pi} \int_{-\infty}^{\infty} \tilde{f}_1(y)\tilde{f}_2(\beta - l) dl. \end{aligned} \quad (2.56)$$

The δ function is defined by

$$\delta(x) = \begin{cases} \infty, & \text{if } x = 0; \\ 0, & \text{otherwise.} \end{cases} \quad (2.57)$$

The convolution integral is simplified by the δ function. The resulting expression for \tilde{f}_y is

$$\tilde{f}_y = -\frac{jd}{2} \left[e^{jq\pi/2} \operatorname{sinc} \left(\frac{\beta d}{2} - \frac{q\pi}{2} \right) - e^{-jq\pi/2} \operatorname{sinc} \left(\frac{\beta d}{2} + \frac{q\pi}{2} \right) \right]. \quad (2.58)$$

To simplify (2.60), note that the exponentials can be represented by

$$\begin{aligned} e^{jq\pi/2} &= (j)^q \\ e^{-jq\pi/2} &= (-j)^q. \end{aligned} \quad (2.59)$$

The expression for \tilde{f}_y becomes

$$\tilde{f}_y = -\frac{jd}{2} \left[(j)^q \operatorname{sinc} \left(\frac{\beta d}{2} - \frac{q\pi}{2} \right) - (-j)^q \operatorname{sinc} \left(\frac{\beta d}{2} + \frac{q\pi}{2} \right) \right]. \quad (2.60)$$

The two transform equations (2.54) and (2.60) are combined to yield \tilde{E}_{x_n} :

$$\begin{aligned} \tilde{E}_{x_n} &= \frac{-bd\pi}{4} (j)^{p+1} (-1)^p J_p \left(\frac{\alpha b}{2} \right) \\ &\quad \left[(j)^q \operatorname{sinc} \left(\frac{\beta d}{2} - \frac{q\pi}{2} \right) - (-j)^q \operatorname{sinc} \left(\frac{\beta d}{2} + \frac{q\pi}{2} \right) \right]. \end{aligned} \quad (2.61a)$$

Similarly the result for \tilde{E}_{y_n} is

$$\begin{aligned} \tilde{E}_{y_n} &= \frac{-bd\pi}{4} (j)^{p+1} (-1)^p J_p \left(\frac{\beta d}{2} \right) \\ &\quad \left[(j)^q \operatorname{sinc} \left(\frac{\alpha b}{2} - \frac{q\pi}{2} \right) - (-j)^q \operatorname{sinc} \left(\frac{\alpha b}{2} + \frac{q\pi}{2} \right) \right]. \end{aligned} \quad (2.61b)$$

Subsectional Basis Functions

The subsectional basis functions used are called rooftop functions since they are composed of triangles in one direction and pulses in the orthogonal direction [17],[18]. As was the case with the full domain basis functions, only

the \mathbf{E}_x basis function will be discussed. Figure 2.6(a) shows a single rooftop basis function located at a position (x_n, y_n) in the aperture. As was discussed in the full sectional case, the electric field in the x -direction goes to 0 at $y = \pm \frac{d}{2}$ and peaks at $x = \frac{b}{2}$. Thus the rooftop functions for \mathbf{E}_x are placed with the roof line parallel to the x axis to best model the field. Figure 2.6(b) shows the layout of the pulses spaced D_x apart. N_x is the total number of pulse functions in the x -direction. Figure 2.6(c) illustrates the N_y overlapping triangles each having a base width of D_y . The pulse and triangle functions $P_{D,x_0}(x)$ and $\Delta_{D,y_0}(y)$ with centers x_0 and y_0 are defined as

$$P_{D,x_0}(x) = \begin{cases} 0, & \text{for } |x - x_0| > \frac{D}{2}; \\ 1, & \text{for } |x - x_0| \leq \frac{D}{2}. \end{cases} \quad (2.62)$$

$$\Delta_{D,y_0}(y) = \begin{cases} 0, & \text{for } |y - y_0| \geq \frac{D}{2}; \\ 1 - \frac{2|y - y_0|}{D}, & \text{for } |y - y_0| \leq \frac{D}{2}. \end{cases} \quad (2.63)$$

A single rooftop electric field basis function is defined by

$$E_{x_n}(x, y) = P_{D_x, x_n}(x) \Delta_{D_y, y_n}(y). \quad (2.64)$$

The pulse and triangle base widths are

$$D_x = \frac{b}{N_x} \quad \text{and} \quad D_y = \frac{2d}{N_y + 1}. \quad (2.65)$$

The basis number, n , is related to the rooftop basis function center (x_n, y_n) by a basis function layout scheme.

The Fourier transform of the basis function (2.64) is obtained from the transforms of the centered pulse and triangle combined with the shift property in the space domain. The transform relations of interest are

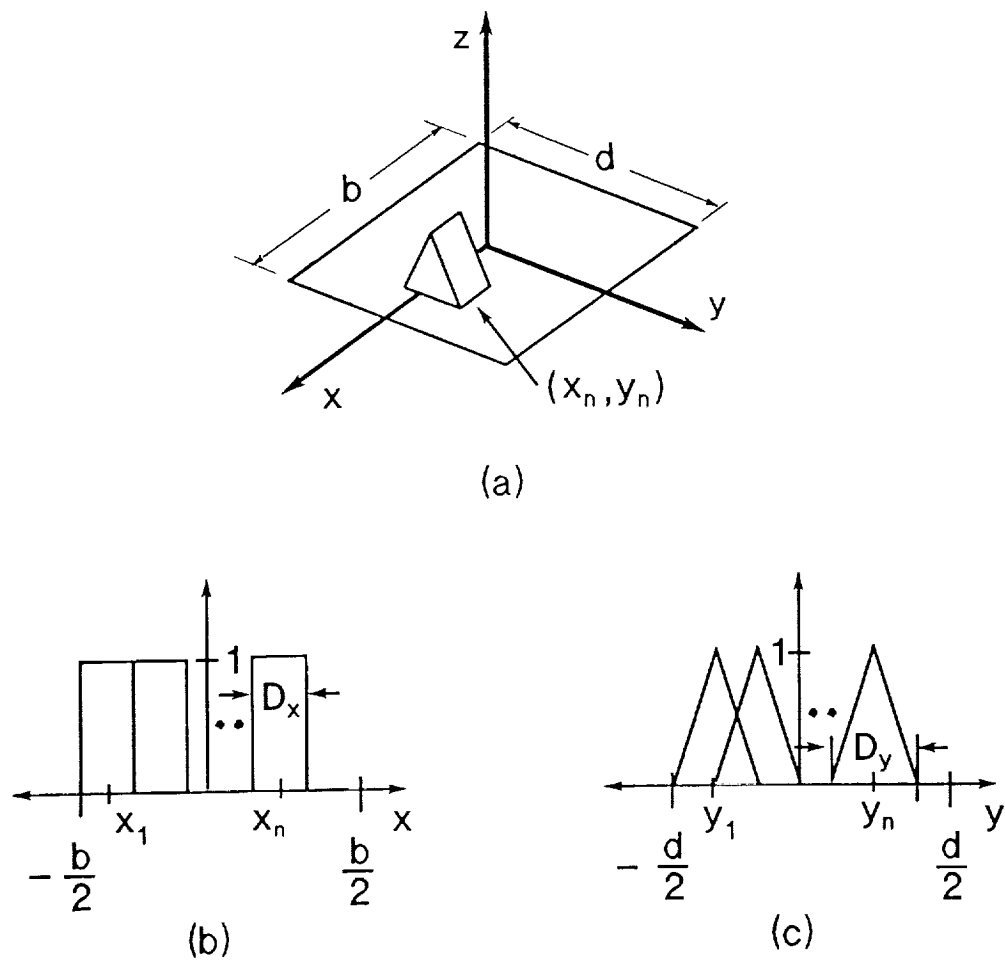


Figure 2.6. Subsectional basis functions for the E_x aperture field.

- (a) Single rooftop function with center (x_n, y_n) .
- (b) Pulse function layout.
- (c) Overlapping triangle functions.

$$\begin{aligned}
P_{D_x,0}(x) &\Rightarrow D_x \operatorname{sinc}\left(\frac{\alpha D_x}{2}\right) \\
\Delta_{D_y,0} &\Rightarrow \frac{D_y}{2} \operatorname{sinc}^2\left(\frac{\beta D_y}{4}\right) \\
f(x - x_0) &= \tilde{f}(\alpha) e^{j\alpha x_0} \\
f(y - y_0) &= \tilde{f}(\beta) e^{j\beta y_0}.
\end{aligned} \tag{2.66}$$

From the relations given in (2.66), the Fourier transform of E_{x_n} is

$$\tilde{E}_{x_n}(\alpha, \beta) = \frac{D_x D_y}{2} \operatorname{sinc}\left(\frac{\alpha D_x}{2}\right) \operatorname{sinc}^2\left(\frac{\beta D_y}{4}\right) e^{j(\alpha x_n + \beta y_n)}. \tag{2.67}$$

The above equation can be used to find the E_y basis functions if the following substitutions are made: $x \leftrightarrow y$, $\alpha \leftrightarrow \beta$, $b \leftrightarrow d$, and $n_x \leftrightarrow n_y$.

2.5 Transmission Coefficient

The planar FSS's transmission coefficient as a function of frequency and incident angle is a principal means of characterizing the behavior of the FSS. In typical operating modes, a single plane wave is transmitted. However, at some frequency above resonance, and or at large incident angles θ , other transmitted modes appear. This effect, which can be compared to grating lobes in a phased array, is called the Wood's Anomaly. Thus, in general a number of transmission coefficients, corresponding to each propagating mode, must be calculated. The magnitude of the transmission coefficient will be found by first defining the total transmission coefficient in the spatial domain. Then, by invoking Parseval's theorem the power transmission coefficient of each propagating wave will be determined.

Referring to Fig. 2.2, the magnitude of the total transmission coefficient, $|T|$, is defined as the power transmitted normally through the FSS, P_{trans} , divided by the power incident normally on the surface, P_{inc} . The expression for $|T|$ is

$$|T| = \frac{\text{Re} \int \int_{\text{aper}} (\mathbf{E}_a \times \mathbf{H}_a) \cdot (-\mathbf{a}_z) da}{\text{Re} \int \int_{\text{cell}} (\mathbf{E}^{\text{inc}} \times \mathbf{H}^{\text{inc}}) \cdot (-\mathbf{a}_z) da}. \quad (2.68)$$

\mathbf{E}_a and \mathbf{H}_a are the total fields in the aperture related by

$$-j\omega\mu\mathbf{H}_a = \nabla \times \mathbf{E}_a. \quad (2.69)$$

From the above equation, the magnitudes of the aperture fields are related by the impedance of free space, Z_0

$$|\mathbf{E}_a| = Z_0 |\mathbf{H}_a|. \quad (2.70)$$

The numerator of (2.68) can be simplified by (2.70) to yield

$$P_{\text{trans}} = \int_{-\frac{b}{2}}^{\frac{b}{2}} \int_{-\frac{d}{2}}^{\frac{d}{2}} \frac{1}{Z_0} |\mathbf{E}_a|^2 \cos \theta dx dy. \quad (2.71)$$

The total aperture electric field, \mathbf{E}_a , is composed of the electric field in the plane of the aperture, \mathbf{E} , and an unknown E_z component. Given that the propagation vector for the radiated plane wave is \mathbf{k}^p , the electric field must satisfy

$$\mathbf{E}_a \cdot \mathbf{k}^p = 0 \quad (2.72)$$

E_z can be found as

$$E_z = \frac{-(E_x k_x^p + E_y k_y^p)}{k_z^p}. \quad (2.73)$$

The integral (2.71) can be simplified by the Parseval's relation for periodic signals [19]

$$\frac{1}{X_0 Y_0} \int_{X_0} \int_{Y_0} |\mathbf{A}(x, y)|^2 dx dy = \sum_m \sum_n \left| \tilde{\mathbf{A}}(\alpha(m), \beta(n)) \right|^2, \quad (2.74)$$

where X_0 and Y_0 correspond to the period of the function in the x and y -directions, respectively. The integral in (2.71) can be simplified by Parseval's theorem with $X_0 = a$ and $Y_0 = c$. The result is

$$P_{trans} = \frac{1}{Z_0} ac \cos \theta \sum_{(m_p, n_p)} \left| \tilde{\mathbf{E}}_a(\alpha(m_p), \beta(n_p)) \right|^2, \quad (2.75)$$

where θ is the angle between the propagation vector of a given plane wave and the $-z$ -axis, and the summation is taken for pairs of (m_p, n_p) corresponding to propagating modes. The propagating modes are found from the field variation along the z -axis, $e^{-jk_z z}$. The propagation constant k_z must be positive for power to be transmitted, where k_z is defined as

$$k_z = \sqrt{k^2 - \alpha^2(m) - \beta^2(n)}. \quad (2.76)$$

Each propagating mode must have the pair (m_p, n_p) satisfying the inequality

$$k^2 > \alpha^2(m_p) + \beta^2(n_p). \quad (2.77)$$

Returning to (2.68), the denominator, P_{inc} , represents the power incident on a unit cell. From the incident geometry, shown in Fig. 2.2,

$$P_{inc} = ac |\mathbf{E}^{inc}| |\mathbf{H}^{inc}| \cos \theta = Z_0 ac |\mathbf{H}^{inc}|^2 \cos \theta. \quad (2.78)$$

The power transmission coefficient for each transmitted mode found by dividing (2.75) by (2.78) is

$$|T(m_p, n_p)| = \frac{|\tilde{\mathbf{E}}_a(\alpha(m_p), \beta(n_p))|^2}{Z_0^2 |\mathbf{H}^{inc}|^2}. \quad (2.79)$$

The phase of the transmission coefficient is the phase change of the incident wave upon transmission through the FSS in a direction given by $\alpha(m_p)$ and $\beta(n_p)$. If Φ is the phase of the incident plane wave and Ψ is the phase of the Fourier transform of the aperture electric field in the direction of interest, then the phase of the transmission coefficient is $\Phi + \Psi$.

CHAPTER 3

LOCALLY PLANAR TECHNIQUE

3.1 Introduction

The LPT, introduced in Chapter 1, is an approximate technique which applies the infinite FSS theory to general FSS shapes with arbitrary incidence subject to some constraints. Before beginning the LPT study, it is worth mentioning the types of FSS problems which have been numerically solved to date. The finite FSS problem can be solved by calculating each aperture's field distribution by matrix inversion for a small number of apertures or by iterative techniques for a large number of apertures [20]. The analysis of the general curved FSS is quite difficult. The curved FSS analysis presented in the literature has been for the case of patches located on a cylindrical surface [21],[22]. The numerical analysis for problems like the hyperbolic subreflector is extremely complex and it appears the LPT may provide the only feasible solution for this type of FSS problem.

In this chapter, the LPT will be developed by applying the theory to the problem of determining the forward scattered field pattern from a generally shaped inductive FSS with arbitrary illumination. Figure 3.1 illustrates the overall geometry and defines the coordinates. In Region I, the incident fields on the FSS are determined from a feed source model. In Region II, the FSS is broken up into N subarrays, each of which is considered to be locally planar. The coordinate system $(X'(n), Y'(n), Z'(n))$ is the local coordinate frame for each subarray specified by n . Invoking the infinite FSS theory at each subarray yields the approximate aperture electric field. The forward scattered far fields are determined in Region III from the Fourier transforms of the aperture fields. The scattered field at the point (x_s, y_s, z_s) is found by summing up the fields radiated from each subarray. In Chapter 5, the LPT will be compared with

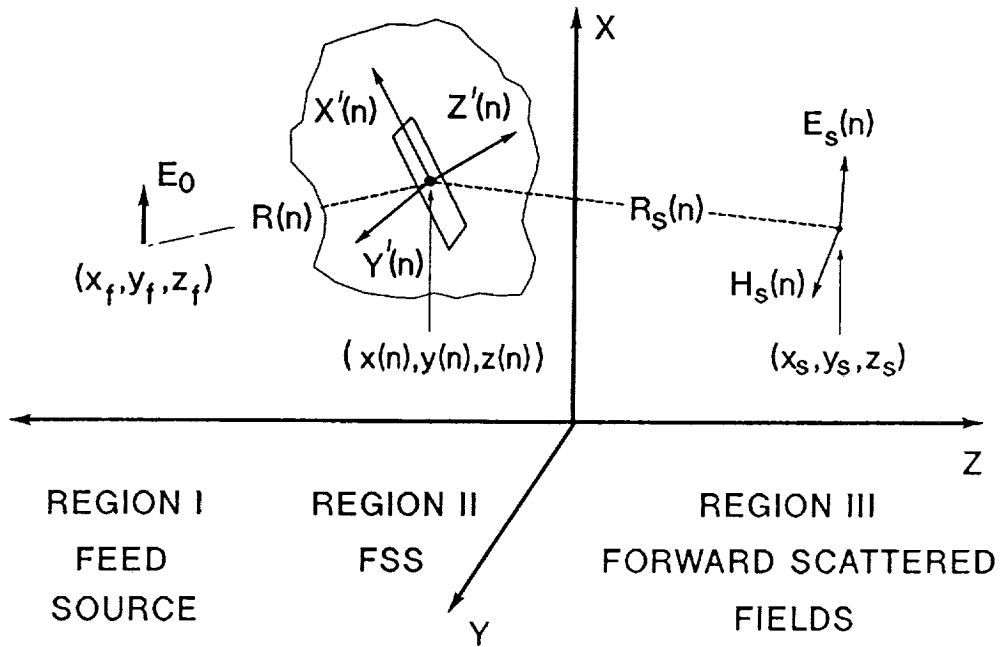


Figure 3.1. Locally planar technique geometry overview for the n^{th} subarray.

experimental results to determine the limitations of the theory.

3.2. Region I. - Feed Source

The feed source radiates a linearly polarized field with the electric field oriented parallel to the x -axis. The feed phase center is located at (x_f, y_f, z_f) . For the experiment, the feed chosen was a pyramidal horn with equal beamwidths in the x - z and y - z planes. The experimental feed pattern was closely modeled in amplitude by a $\cos^m \theta_1 \cos^m \theta_2$ approximation. Figure 3.2 illustrates the feed geometry. The calculated and measured feed pattern for a value of $m = 2.355$ is shown in Fig. 3.3. The solid line is the cosine numerical approximation. The dashed line and dotted line are the H-plane and E-plane measured patterns, respectively. In all experiments, the FSS is in the far field of the transmit horn. Thus, the magnitude and phase of the incident field at each subarray n on the FSS can be modeled by

$$E^{inc}(n) = \frac{E_0}{R(n)} \cos^m \theta_1 \cos^m \theta_2 e^{-jk_0 R(n)}. \quad (3.1)$$

$R(n)$ is the distance from the feed phase center to the location of each subarray. The incident electric field in the global coordinate frame, (X, Y, Z) , is $E^{inc}(n)$ where

$$\begin{aligned} E_x &= E^{inc}(n) \cos \theta_1 \\ E_y &= E^{inc}(n) \sin \theta_1 \sin \theta_2 \\ E_z &= -E^{inc}(n) \sin \theta_1 \cos \theta_2. \end{aligned} \quad (3.2)$$

The components of the incident propagation vector are

$$\begin{aligned} k_x &= k_0 \sin \theta_1 \\ k_y &= k_0 \cos \theta_1 \sin \theta_2 \\ k_z &= k_0 \cos \theta_1 \cos \theta_2. \end{aligned} \quad (3.3)$$

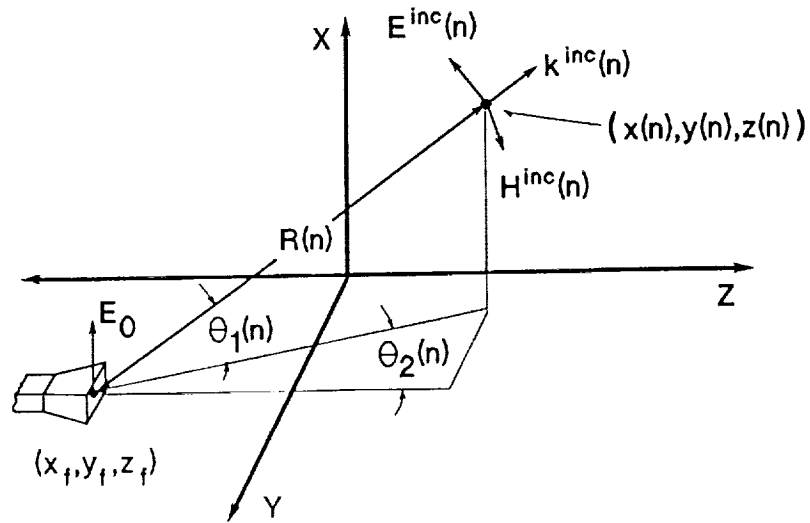


Figure 3.2. Pyramidal horn feed geometry.

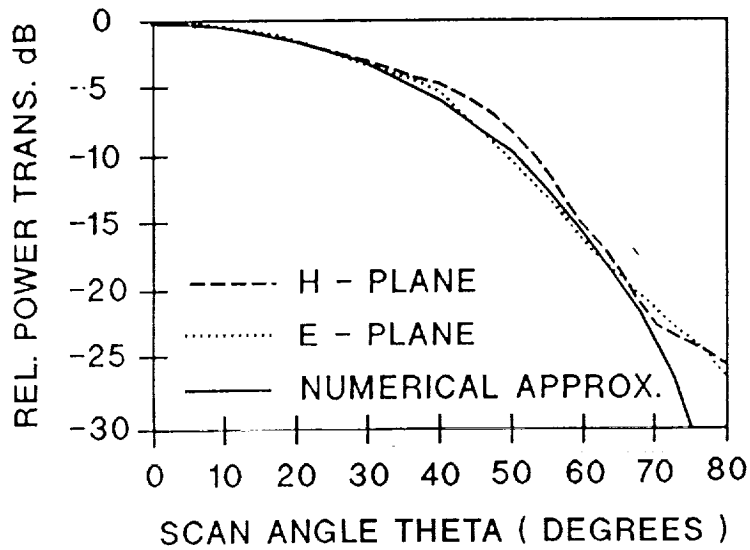


Figure 3.3. Pyramidal horn approximate numerical and experimental patterns.

From Fig. 3.2 the incident magnetic field is

$$\mathbf{H}^{inc}(n) = \frac{\mathbf{k}^{inc}(n) \times \mathbf{E}^{inc}(n)}{Z_0 k_0}, \quad (3.4)$$

where Z_0 is the impedance of free space.

3.3. Region II. - Inductive FSS

The general shaped FSS is first divided into N subarrays. Each subarray is made up of one or more apertures. Ideally, the subarray should be a single aperture in size. This is because the smaller the subarray, the more accurately the surface geometry and incident field contour is represented. The main reason to use subarrays composed of many apertures is to reduce the number of infinite FSS calculations, and hence the CPU time. In the analysis which follows, the subarray is composed of a single aperture and N represents the number of apertures in the FSS.

At each aperture location, shown in Fig. 3.1, the aperture electric field is calculated from the infinite inductive FSS analysis with the plane of the FSS positioned tangent to the surface at the aperture center. The necessary incident field parameters are the incident magnetic field and the propagation vector. The incident quantities are determined by projecting the incident vectors found in the previous section into the aperture plane. The procedure is repeated for each aperture on the FSS. From the aperture fields, the scattered far fields from the general surface can be determined.

3.4. Region III - Forward Scattered Fields

One method to calculate the transmitted scattered field is by integrating the magnetic currents in the spatial domain. This type of field calculation was shown by Ko and Mittra in their study of a parabolic cylinder [4]. However, since the Fourier transforms of the magnetic currents and aperture electric fields are available, there is no need to perform a spatial integration to obtain the far fields. The radiated fields can be found conveniently from the transforms of

the electric field basis functions. The radiation in a given direction is specified by the transmission propagation vector \mathbf{k} . Fig. 3.4 illustrates the components of the propagation vector in the local aperture plane. Also shown are the θ' and ϕ' direction angles. For a given aperture n , the Fourier transform of the electric field in the plane of the aperture is

$$\tilde{\mathbf{E}}(k_{x'}, k_{y'}) = \tilde{E}_{x'}(k_{x'}, k_{y'})\mathbf{a}_{x'} + \tilde{E}_{y'}(k_{x'}, k_{y'})\mathbf{a}_{y'}, \quad (3.5)$$

where $(k_{x'}, k_{y'})$ are the transform variables in the local coordinate system for the n^{th} aperture. The forward scattered far field expressed in the local coordinates is [23]:

$$\begin{aligned} \mathbf{E}_s = jk_0 \frac{e^{-jk_0 R_s}}{2\pi R_s} & \left[\mathbf{a}_{\theta'} \left(\tilde{E}_{x'}(k_{x'}, k_{y'}) \cos \phi' + \tilde{E}_{y'}(k_{x'}, k_{y'}) \sin \phi' \right) \right. \\ & \left. + \mathbf{a}_{\phi'} \cos \theta' \left(\tilde{E}_{y'}(k_{x'}, k_{y'}) \cos \phi' - \tilde{E}_{x'}(k_{x'}, k_{y'}) \sin \phi' \right) \right]. \end{aligned} \quad (3.6)$$

The forward scattered field region is illustrated in Fig. 3.5. The scattered field pattern is measured by choosing an angle ϕ in the global coordinate system and scanning θ through the desired scan range. The receive probe remains pointed at the origin of the global coordinate system throughout the scan. The angle between the propagation vector from an aperture n and centerline of the horn is $\theta_p(n)$. At each scan point, (x_s, y_s, z_s) , the received electric field is separated into the θ and ϕ global coordinates. The receive probe in the experiment was an open ended cylindrical waveguide with an antenna pattern modeled by

$$\mathbf{E}(\theta_p) = E_0 \cos^n \theta_p \quad (3.7)$$

E_0 is the magnitude of the electric field in the direction of the polarization of the probe. Depending on which polarization is desired, the horn is rotated for

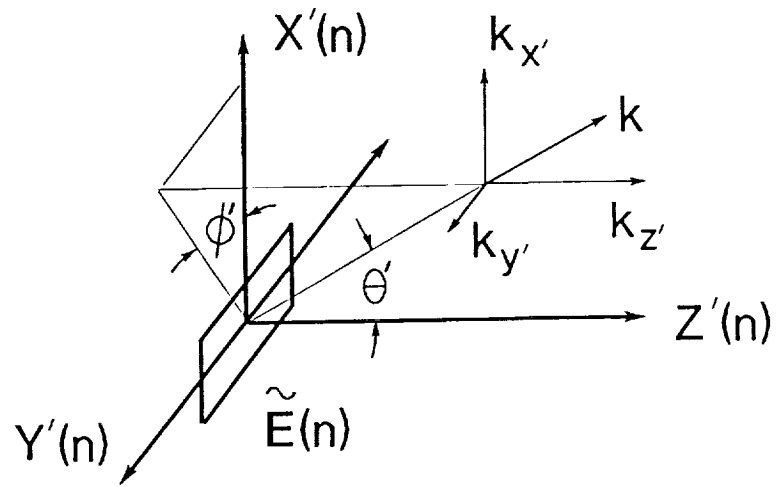


Figure 3.4. Forward scattered field propagation vector and local aperture coordinate system.

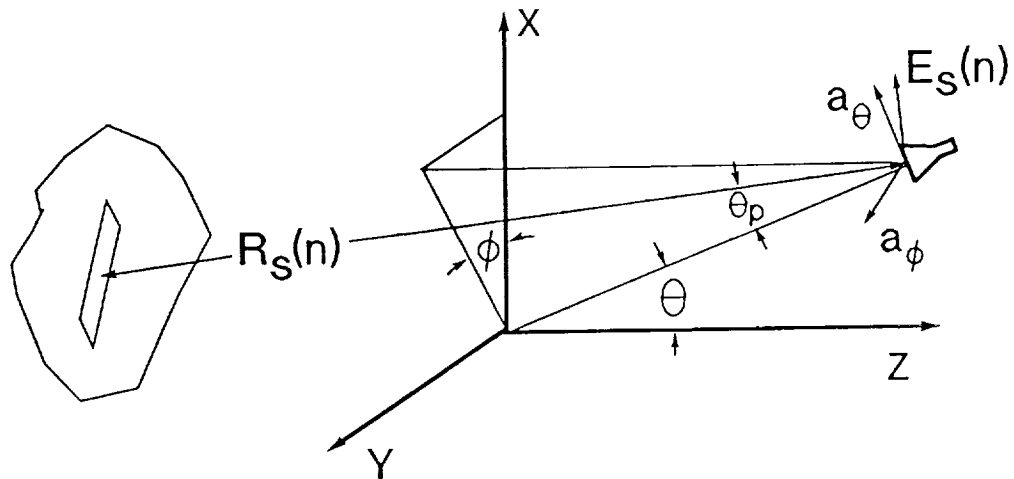


Figure 3.5. Forward scattered field receive probe and global coordinate system.

E_θ or E_ϕ orientation. The received electric field, E_θ or E_ϕ , is the summation of the contributions from each aperture modified by the receive probe's antenna pattern. As a note, if the scan angles are large and the surface is sufficiently curved, there will be a point where some of the apertures will no longer be visible. The radiation contribution from these apertures is set equal to zero.

3.5. - Locally Planar Theory Summary

The combination of the LPT and the spectral domain FSS analysis is an efficient technique for finding the approximate radiation pattern for complex FSS geometries. In Chapter 5, the LPT theory will be compared to results from an experimental study. The accuracy and applicability of the approach will be addressed in terms of incident wavefront and FSS curvature.

CHAPTER 4

FREQUENCY RESPONSE OF THE INDUCTIVE FSS: NUMERICAL AND EXPERIMENTAL RESULTS

4.1 Inductive FSS Design

The FSS was experimentally studied at the NASA Goddard Space Flight Center (GSFC) from 1987 - 1989 as a part of the thesis study effort. The results from the studies have proved valuable for comparison with the theories developed in Chapters 2 and 3. The experiments included frequency response as well as scattered field pattern measurements. In this chapter, the transmission coefficient experiments and results for the infinite inductive FSS composed of rectangular apertures will be presented.

In the past, inductive FSSs have been constructed at GSFC by punching apertures in an aluminum sheet. In previous years, it was necessary to control the punching machine by hand to place each aperture in the proper position. Fortunately, a new computer-controlled punching machine was available at the shop and this was ideal for fabricating the FSS. The experimental FSS's overall size was chosen to be .6 m square. For the infinite FSS theory to accurately model the experimental FSS, a large number of apertures is necessary. Initially, S-band (2-4 GHz) was considered. However, at this frequency only about 12 apertures could fit on the sheet. Moving up in frequency, the range of 9-13 GHz was chosen because a large number (≈ 600) of apertures would fit on the FSS sheet and test equipment was readily available in this band. A frequency of 11 GHz, the center of the range, was selected as the resonant frequency for the experimental FSS.

The FSS aperture dimensions and spacings were designed by the infinite FSS theory presented in Chapter 2 for an incident electric field E_x . The FSS aperture dimension d , shown in Fig 2.1, was initially chosen to be half a wave-

length in size at the resonant frequency. The desired frequency response was one which was narrow enough for easy identification of the resonant frequency. The aperture size b is the principal means for changing the transmission bandwidth. From the theory, the larger the aperture dimension b , the larger the transmission bandwidth. The FSS was also designed to place the Wood's Anomaly well above the resonant frequency. In this way, a single transmitted plane wave could be measured to characterize the frequency response of the surface. The Wood's Anomaly frequency depends primarily on the aperture to aperture spacing a . The smaller the value of a , the higher the frequency of the Wood's Anomaly. The choice of a depended primarily on leaving enough metal between the apertures for structural integrity. A standard punch size of 12.7×4.23 mm ($\frac{1}{2} \times \frac{1}{8}$ inch) was finally chosen for the FSS aperture to meet the desired response characteristics. If a non-standard hole size was required, each aperture would be nibbled out with a small punch leaving an undesirable rough scalloped edge. The resonant frequency was fine tuned by varying the dimension c . The dimensions of the apertures and spacings for the experimental inductive FSS are shown in Fig. 4.1.

The FSS thickness needed to be as small as possible to approximate the zero thickness theoretical surface. The thinnest aluminum sheet which could be punched successfully on the punching machine was .5 mm thick. This thickness corresponds to $\frac{\lambda}{50}$, where λ is the resonant frequency. Thus the experimental FSS is a good approximation to the theoretical surface. In later experiments, the thin FSS proved its versatility since it could be shaped into a hyperbolic cylinder and later be released to spring back to a flat surface.

For completeness, the initial test setup for measuring both the transmission coefficient and scattered fields should be mentioned. The original plan was to use the GSFC outdoor antenna range for the FSS tests. Gordon Zeeman and Vic Rinker of the University of Maryland designed and constructed a

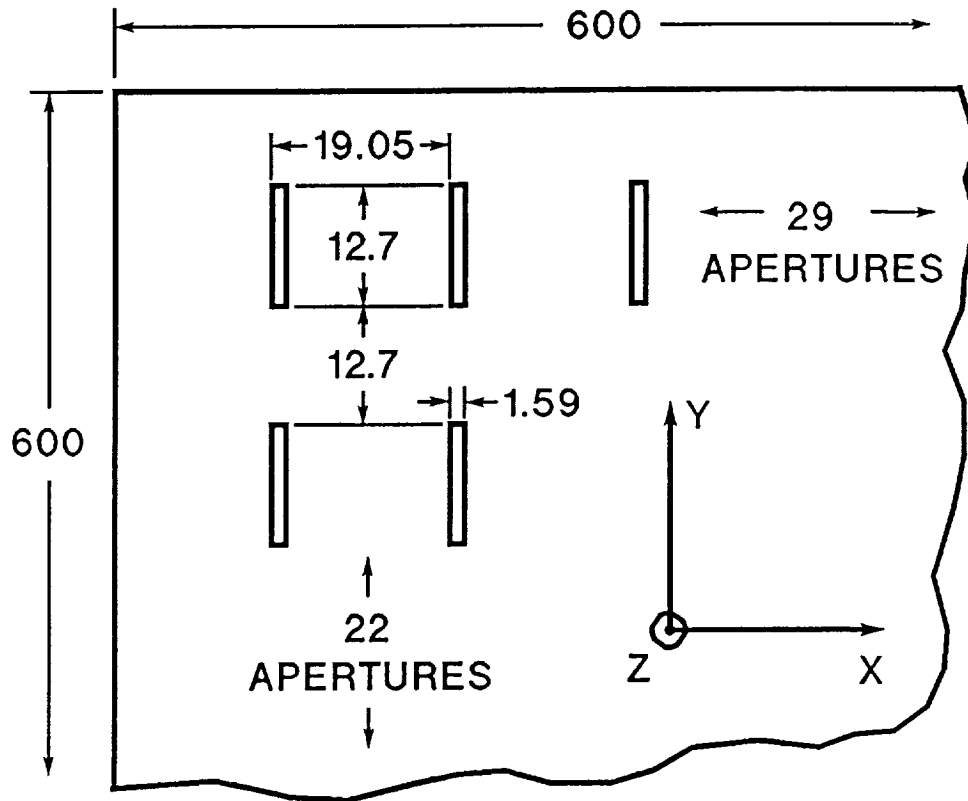


Figure 4.1. Experimental inductive FSS design with 11-GHz resonant frequency. The dimensions are in millimeters and the FSS thickness is .5 mm.

FSS test stand for use with the outdoor range. A number of difficulties such as wind, weather, unknown moisture in the wooden stand, and scattering around the stand caused the outdoor experiment to be abandoned and the experiment was moved inside.

4.2 Transmission Coefficient Magnitude: Numerical and Experimental Results

Figure 4.2 shows a schematic of the FSS experimental configuration used to measure the magnitude of the transmission coefficient. The FSS is positioned at an angle δ to the incident plane wave direction and surrounded by an absorber wall. The orientation of the FSS apertures is given by the coordinate axes shown. The incident electric field from the transmit horn was directed across the narrow dimension of the aperture. The transmit horn was placed a distance $D = 2.1$ m away from the FSS and the receive probe was placed a distance $d = .7$ m from the FSS. The receive probe was a waveguide to coax adapter surrounded by absorber. The test equipment was configured to sweep over the frequency range of interest and the resulting transmission coefficient magnitude versus frequency was outputted via a plotter. An initial test was to determine the dynamic range of the measurement setup. By blocking the FSS area and comparing the signal level to the case of no blockage, a dynamic range of about 20 dB was achieved.

The FSS frequency response was measured by first calibrating the system with the FSS removed. The FSS was placed back in the absorber wall and positioned at an angle $\delta = 0$ for normal plane wave incidence. When the frequency sweep was taken, strong reflections occurred between the FSS and the receive probe. The resulting standing wave is seen as an apparent change of the transmission coefficient as the receive probe is moved through a distance range of half a wavelength. Figure 4.3 illustrates the variation of the response due to the standing wave. The receive probe distance was moved in 6-mm

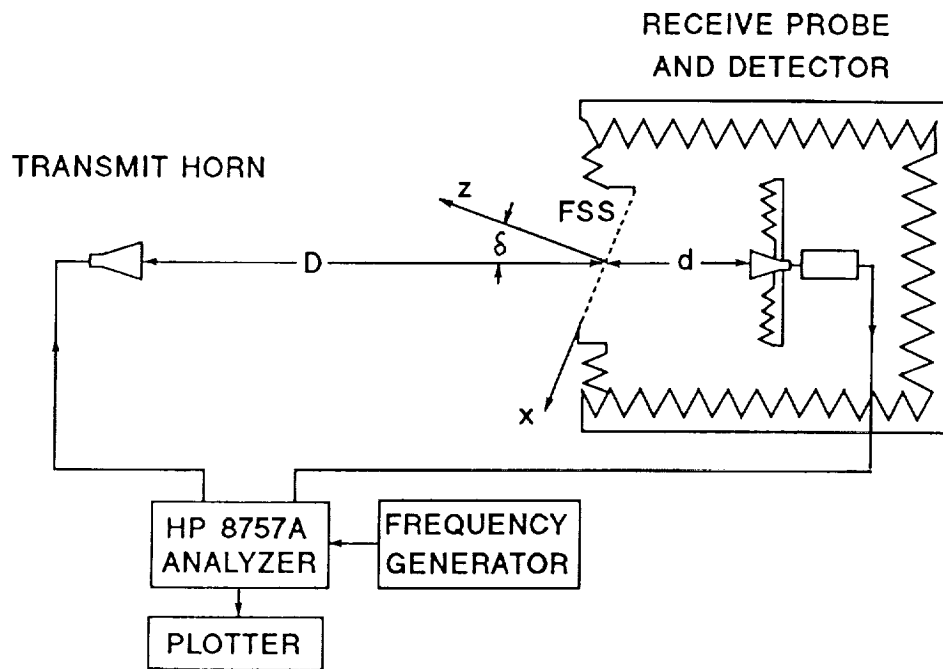


Figure 4.2. Experimental configuration for measuring the magnitude of the transmission coefficient. The incident electric field is in the (x, z) plane. The FSS orientation is given by the x -axis. The FSS dimensions are found in Fig. 4.1.

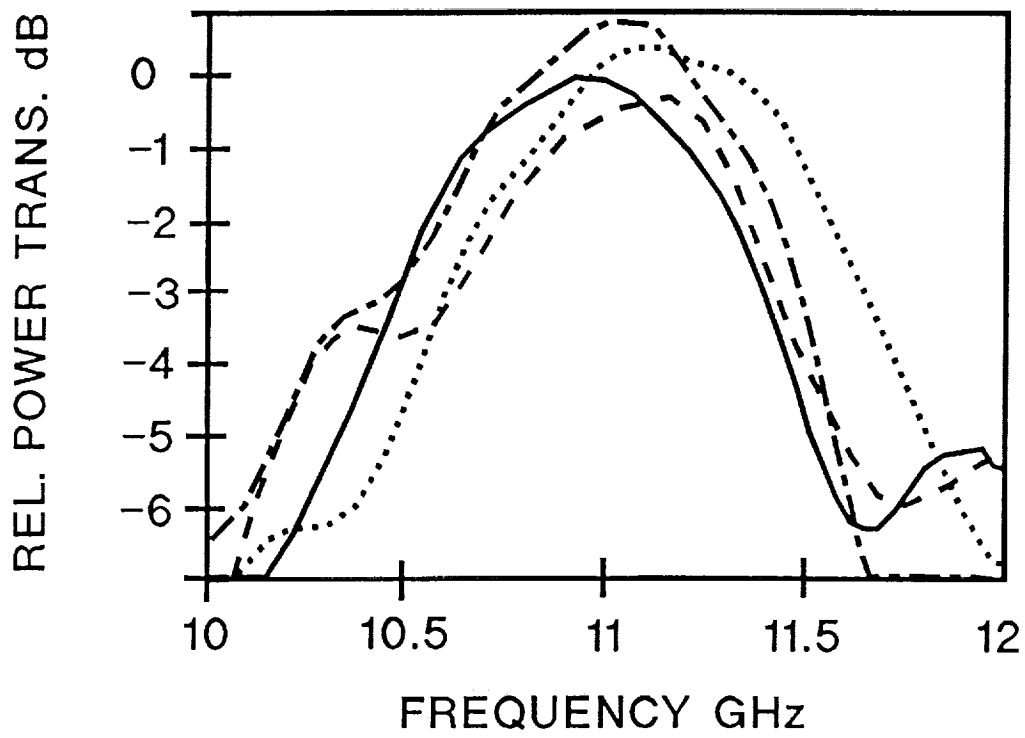


Figure 4.3. Transmission Coefficient variation due to the standing wave. The receive probe was moved in steps of 6 mm about a distance $d = .7$ m to obtain the various curves. The incident electric field is polarized in the x -direction with $\delta = 0$ incidence. The FSS dimensions are found in Fig. 4.1.

steps to produce the different curves shown. The standing wave could be reduced in magnitude by increasing d because with a fixed receiving antenna aperture, the power density at the FSS due to scattering from the receive probe is reduced. Shuley has shown the standing wave perturbation can be removed from the data by averaging the transmission coefficient as the spacing is varied over half a wavelength [24]. This is reasonable if one considers the effect of varying d on the response. The standing wave alternates between a positive and negative contribution to the receive signal as the distance d is varied. Hence the receive power is modulated with respect to distance and can be averaged out.

The solid line in Fig. 4.4 illustrates the averaged experimental transmission coefficient obtained from Fig. 4.3. The dotted curve is the calculated frequency response for the FSS using 4 full domain basis functions in each direction and a large number (101) spectral terms in the inner product summations. Convergence of the solution was established with this number of spectral terms. The concept of relative convergence has been investigated as it applies to the FSS problem. A criterion for the selection of the number of spectral terms has been suggested [25]. If the number of basis functions in the x and y directions are given by n_x and n_y respectively, relative convergence states M and N should be chosen to satisfy

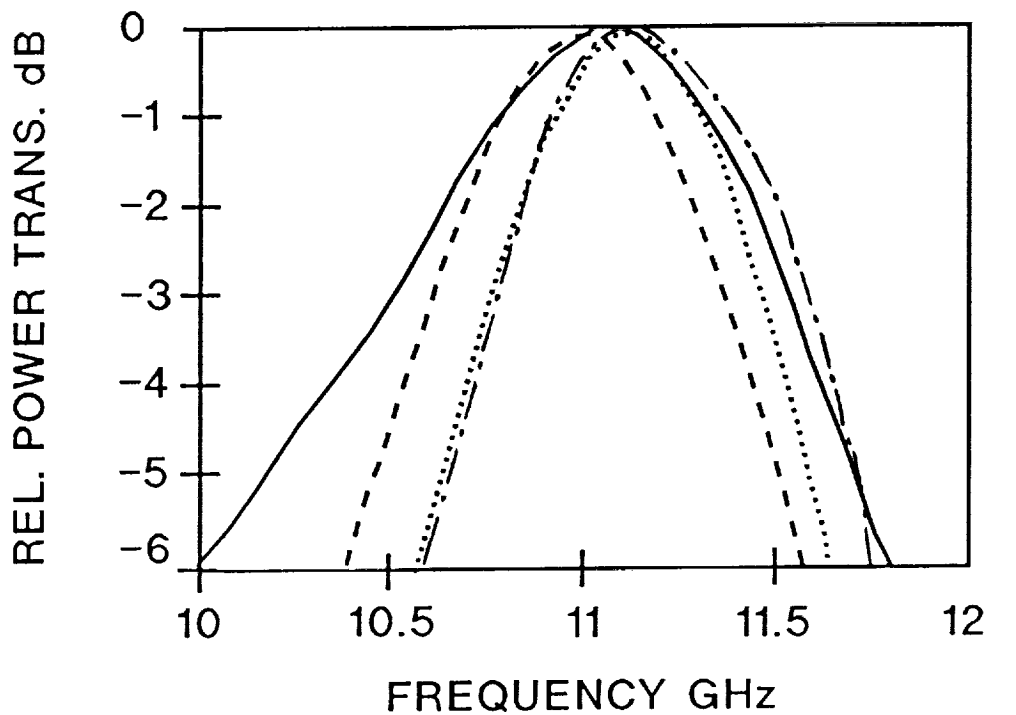
$$\frac{n_x}{M} = \frac{b}{a} \quad (4.1a)$$

$$\frac{n_y}{N} = \frac{d}{c}, \quad (4.1b)$$

where M and N are defined by

$$M = 2m + 1 \quad (4.2a)$$

$$N = 2n + 1. \quad (4.2b).$$



- Subsectional - Rooftop basis functions
- Full domain basis - Relative convergence criterion
- Experiment data average
- Full domain basis - Large number of spectral terms.

Figure 4.4. Experimental and numerical power transmission coefficient as a function of frequency. The incident electric field was polarized in the x -direction with incident angle $\delta = 0$. The FSS dimensions are found in Fig. 4.1.

The constants a and c are the unit cell dimensions and b and d are the aperture dimensions given in Fig. 2.1. The number of basis functions and spectral terms are integer quantities so the equalities in (4.1) and (4.2) can only be approximately met. With the experimental FSS geometry and 4 basis functions in each direction, the relative convergence criteria states $M = 48$ and $N = 8$. The numerical result using (4.1) is shown by the dashed line in Fig. 4.4.

Finally, the subsectional rooftop basis functions were used to solve the FSS problem. The basis function set consisted of 3 basis functions in x and 3 basis functions in y , for a total of 9 basis functions in each direction. The resulting matrix equation had dimensions 18×18 as compared to 8×8 for the full-domain case. A large number of spectral terms, $m = n = 50$, was chosen for the inner product summations. The numerical results are shown by the dot-dashed line in Fig. 4.4. A full discussion of the experimental results and numerical calculations has been presented by Webb, Grounds, and the author [26]. The experimental resonant frequency was found to be 11.05 GHz. The full domain relative convergence solution resonance occurred at about 11.0 GHz and the large number of spectral terms solution resonance occurred at 11.1 GHz. The subsectional basis function solution also resonated at 11.1 GHz. All of the solutions are extremely close to predicting the experimental resonance and the accuracy of the experiment could be on the order of the difference between theory and experiment.

Increasing the angle δ to a non-zero value results in a shifting down of the resonant frequency. Figure 4.5 shows the results of the experiment and the full-domain, large number of spectral terms, numerical solution. Note how the resonance has shifted down to the 10-GHz region. The frequency of the resonance is quite sensitive to the incident angle δ . In the experiment, the error in determining δ was on the order of 2° . Changing δ from 30° to 32° produced a calculated resonance shift of .175 GHz. Thus, the experimental error could

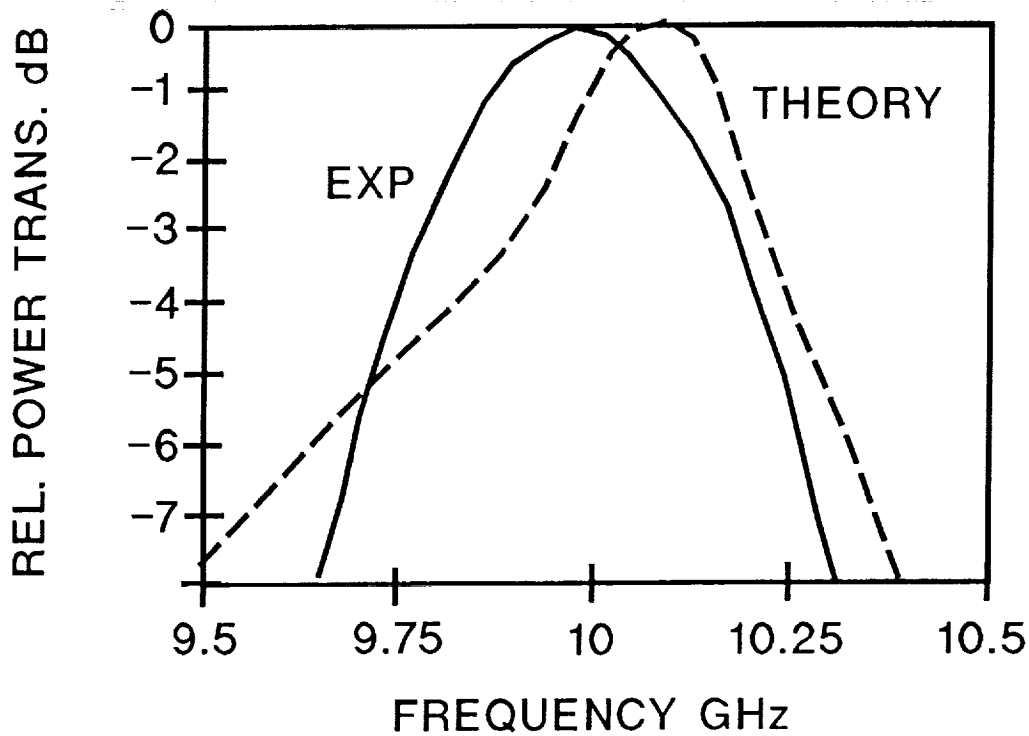


Figure 4.5. Power transmission coefficient for the inductive FSS as a function of frequency. The incident electric field is polarized in the x -direction with $\delta = 30^\circ$. The FSS theory shown is the large number of spectral terms solution. The calculated experimental error is on the order of .175 GHz. The FSS dimensions are found in Fig. 4.1.

be a major part of the difference between experiment and theory.

The experimental FSS discussed represents a very basic filter element. A large variety of aperture geometries have been designed to enhance the filter characteristics of a FSS. Some of the geometries which have been studied in detail are the crossed dipole, Jerusalem cross, and circular aperture [27],[28]. In addition, a number of FSSs can be cascaded to produce the RF equivalent of a multi-pole filter [29]. For accurate results, the evanescent modes must be included in the analysis of the multiple-layered FSSs [30].

4.3 Transmission Coefficient Phase: Numerical and Experimental Results

While the magnitude of the transmission coefficient is extremely useful for characterizing the overall response of the FSS, the phase response is equally as important. For example, if the FSS is used in an antenna system, the FSS amplitude and phase characteristics must be included for accurate antenna pattern results to be obtained. Just as was the case for the magnitude of the transmission coefficient, the phase of the transmitted wave is dependent upon both frequency and angle of incidence.

Figure 4.6 shows the experimental setup for measuring the phase response of the inductive FSS. The testing frequency of interest is fed from the signal generator to the transmit horn. A sample of the signal is attenuated and mixed with a local oscillator signal *from* the receiver to provide a 45-MHz IF reference signal for the receiver. The received signal is picked up by a horn antenna, mixed with the local oscillator, and sent to the receiver. At the receiver, the phase difference between the received signal and the reference is measured. The mixers are located external to the receiver to reduce the large attenuation of microwave signals in the coaxial cable. Once the signal is downconverted to 15 MHz, the coaxial cable loss is small and the receiving antenna can be placed at a distant point from the receiver.

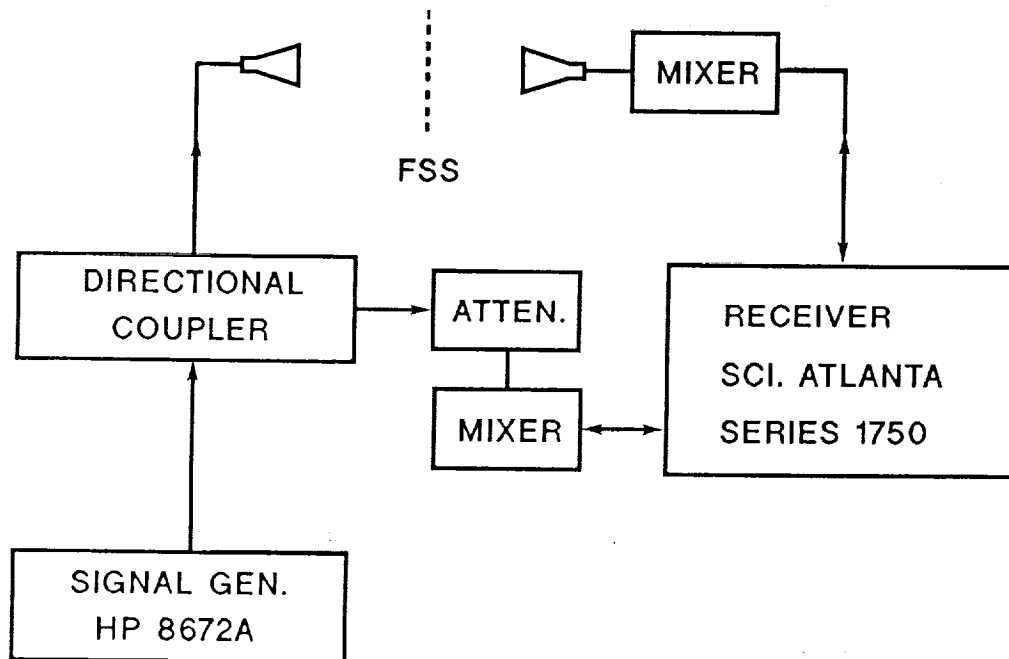


Figure 4.6. Transmission coefficient phase measurement experimental setup.

The phase experiment began by establishing a phase reference between the transmit and receive horn with the FSS removed. The FSS was inserted between the transmit and receive probes and the phase shift, also called the insertion phase, was obtained from a meter on the receiver. The procedure was repeated for a number of frequencies to establish the phase response as a function of frequency. Figure 4.7 is the measured and calculated phase response for the FSS with normal plane wave incidence, $\delta = 0$. Note at resonance the phase shift is equal to zero.

A large number of FSS problems can be solved with the experimental and theoretical results discussed in this chapter given the incident wave is nearly planar and the FSS is large and flat. In the next chapter, the experimental and numerical results for the LPT will be presented as a way to extend the infinite planar theory to general inductive FSS forward scattering problems.

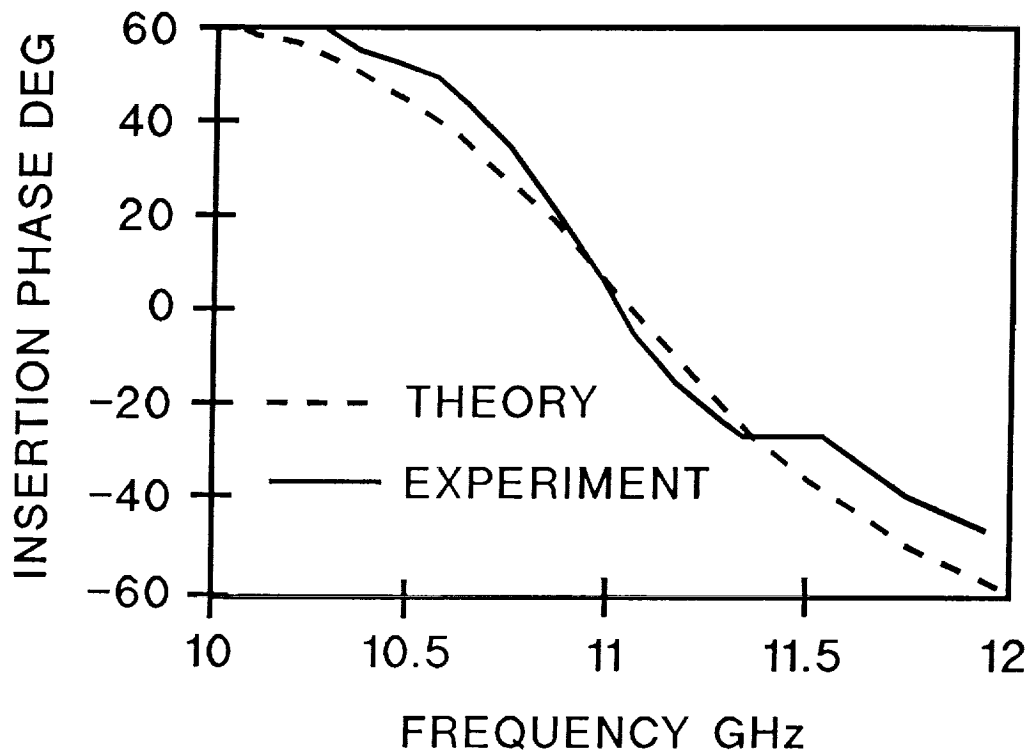


Figure 4.7. Transmission coefficient phase experimental and theoretical results for a frequency of 11 GHz. The incident electric field is polarized in the x -direction and $\delta = 0$. The FSS dimensions are found in Fig. 4.1.

CHAPTER 5

INDUCTIVE FSS FORWARD SCATTERED FIELD EXPERIMENTS AND MODELING

5.1. Introduction

Knowledge of the scattered field from a FSS is important for the design of FSS subreflectors and radomes. Both the reverse (reflected) and forward (transmitted) scattered fields may be necessary for a given FSS problem. In this chapter, the forward scattered field is measured and compared with theory for a number of FSS and feed/receive probe geometries. The forward scattered field was chosen for study because the FSS could be placed in an absorber window for good isolation between the feed and receive probes. If the reverse scattered field had been chosen, at near normal incidence angles, the receive probe would block the illuminating field making it difficult to measure the true backscatter response.

The equipment schematic for measuring the forward scattered field pattern is shown in Fig. 5.1. The basic testing equipment is identical to the equipment used in the Chapter 4 phase measurement study. An antenna positioner and chart recorder have been added to complete the test setup. The testing frequency, if not mentioned otherwise, is 11 GHz. A photograph of the test equipment is shown in Fig. 5.2. In the middle of the left rack is the receiver with cables running to the associated equipment. Directly below, on the bottom of the left rack is the chart recorder. In the center of the console is the antenna positioner and feed horn polarization controls. A number of the experiments were performed in a 15 m anechoic chamber when it was available. The remainder of experiments were conducted in a large laboratory room with microwave absorber blocks situated in appropriate positions to obtain a near anechoic environment.

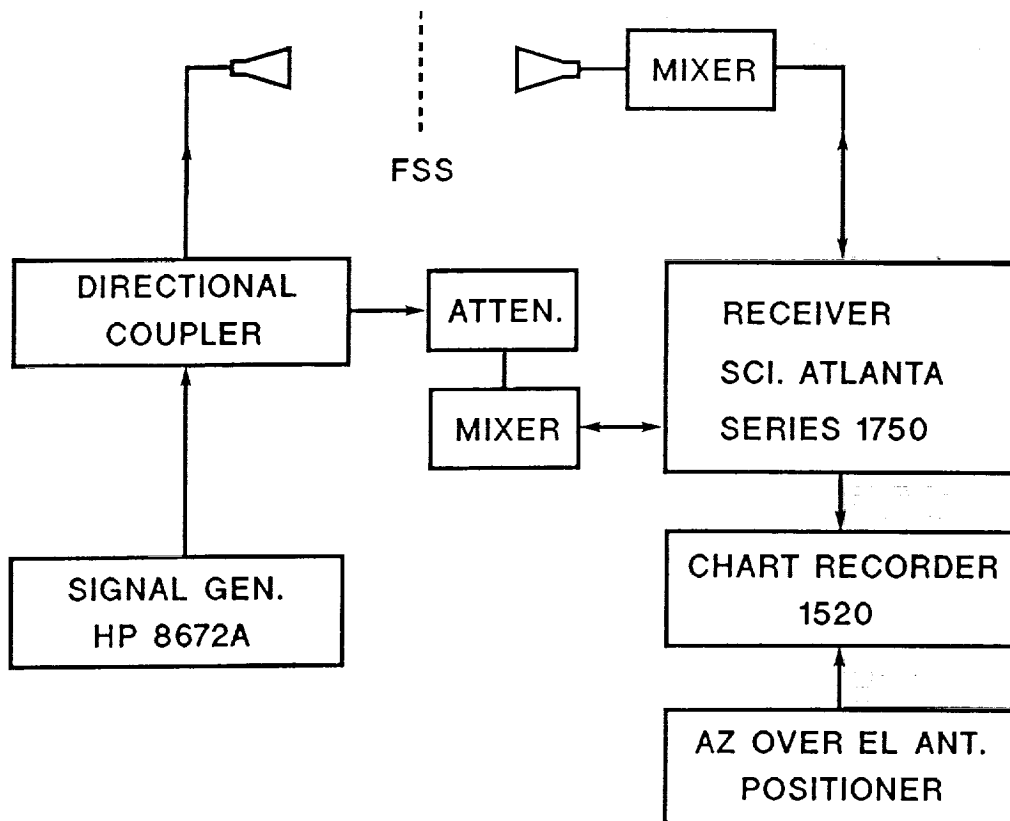


Figure 5.1. Schematic of the test equipment used to obtain the scattered field measurements.

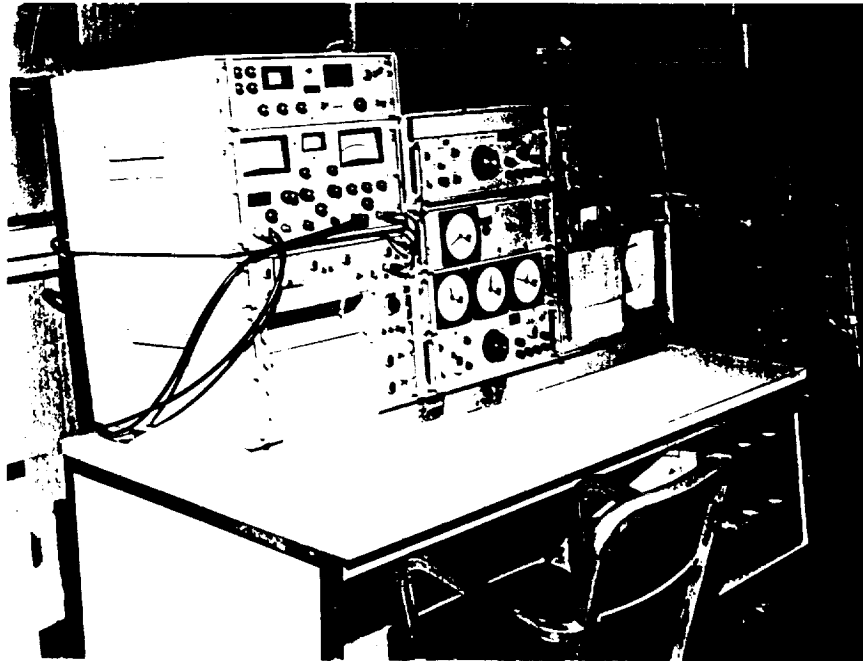


Figure 5.2. Photograph of the Scientific Atlanta antenna pattern measurement equipment.

5.2. Scattered Field Experiments with Plane Wave Incidence on a Planar FSS

The first scattered field experiment, illustrated in Fig. 5.3, was performed in the anechoic chamber. The transmit horn was placed a distance $D = 15$ m from the FSS with polarization shown. The FSS was supported in a large absorber wall positioned at an angle δ from the transmit horn axis. The FSS's orientation is given by the coordinate axes shown. The receive probe, embedded in absorber, was placed on the anechoic chamber's azimuth rotator a distance $d = .8$ m away from the FSS. The receive probe scanned through an angle θ to measure the forward scattered pattern. Figure 5.4 is a photograph of the absorber wall in the anechoic chamber positioned at $\delta = -30^\circ$. The FSS has been removed and the receive probe-absorber is visible thru the window in the absorber wall. Figure 5.5 is a photograph of the receive probe in the forward scattered field area of the experiment. The receive probe is surrounded by absorber and the FSS is located in the absorber wall.

In this experiment, the incident wavefront is nearly planar. Thus each aperture's transmission coefficient is approximately the same. As a first approximation, the forward scattered field from the FSS can be calculated by the array factor. The array factor pattern is given by a superposition of the fields from point sources located at the center of each aperture. The point sources are excited with an amplitude and phase corresponding to the incident field at the location of the point source. Since the element pattern is broad compared to the array factor, the latter dominates the scattered field response.

The FSS was masked with conducting foil to cover all the apertures except for a strip, 3 apertures wide, centered along the y -axis. By choosing a limited number of apertures, the sidelobe structure of the array became distinct and comparison of theory and experiment was made much easier. Figure 5.6 shows the scattered field experimental and numerical results for the case of 3 aper-

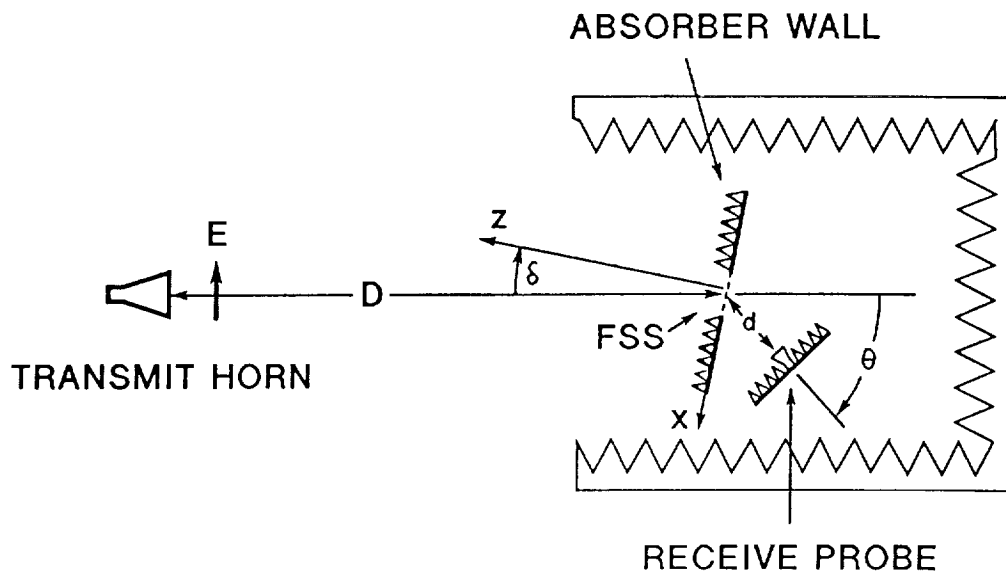


Figure 5.3. Schematic of the anechoic chamber experiment for plane wave incidence - planar FSS forward scattered field measurements. The FSS aperture orientation is given by Fig. 2.1.

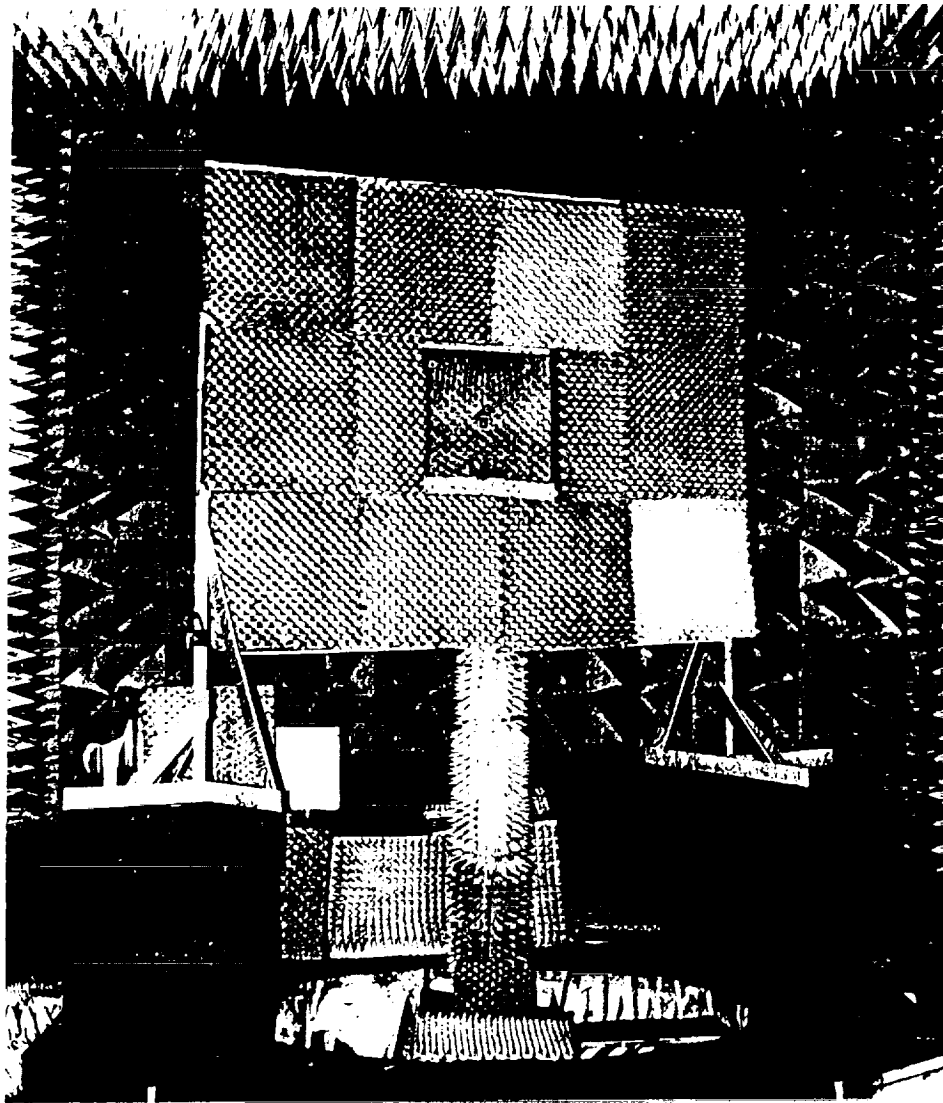


Figure 5.4. Absorber wall positioned at $\delta = -30^\circ$ in the anechoic chamber. The FSS has been removed and the receive probe area is visible.



Figure 5.5. Photograph from the transmitted scattered field region area of the experiment showing the FSS and the receive probe on the rotating positioner.

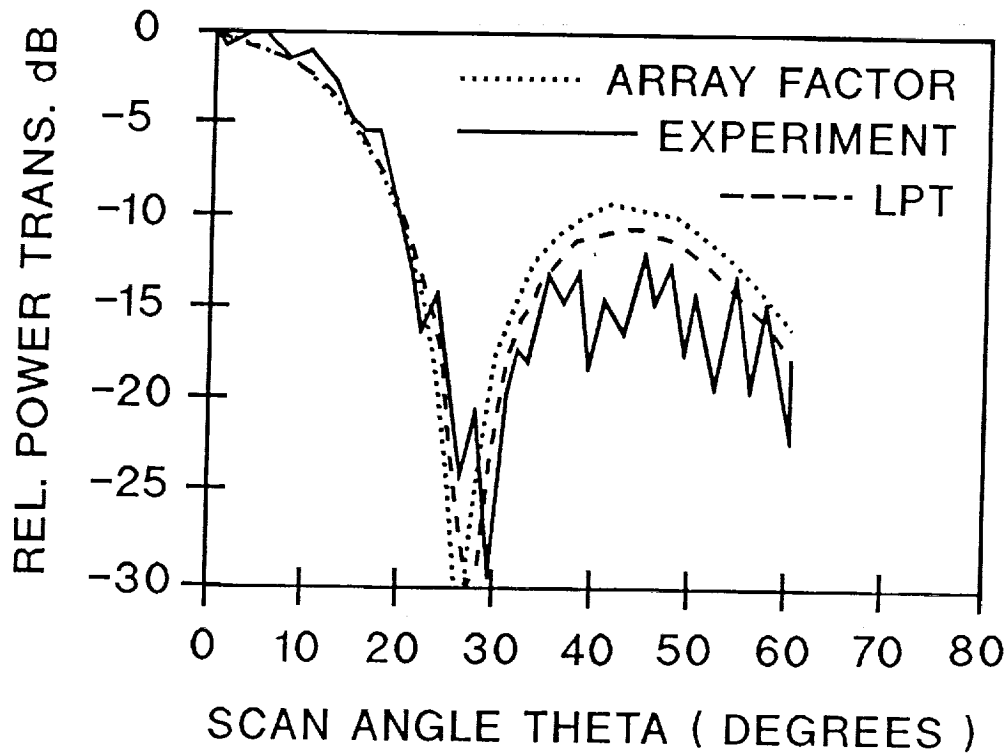


Figure 5.6. Forward scattered field pattern for $\delta = 0$ plane wave illumination on a FSS with 3 apertures in the x -direction and 22 apertures in the y -direction. The test frequency was 11 GHz, θ is in the (x, y) plane, and the incident electric field is E_x .

tures in the x -direction and 22 apertures in the y -direction. The FSS was positioned at an angle $\delta = 0$. The experimental scattered field measurement is shown by the solid line. The dotted line is the array factor approximation. The dashed line is the result using the LPT approach from Chapter 4. The LPT takes into account the aperture's element pattern resulting in a close agreement between the LPT results and the experimental data. In all of the scattered field experiments, the maximum received power from the experiments and numerical calculations is normalized to 0 dB. A number of other experiments with different aperture masking and orientation angle δ were explored with the array factor approximation method. In general, the array factor predicted the scattered field peaks and nulls quite well. The results are presented in the paper *Finite and Infinite Frequency Selective Surfaces: Experiment and Models* by Caroglanian et al. [31].

In the forward scattering experiment discussed, only a single plane wave was incident upon the FSS surface. To explore the forward scattered field response of the FSS for plane waves incident at different angles, the experiment illustrated in Fig. 5.7 was configured. In this setup, the feed remained the same, however, now both the FSS and receive probe rotate as a unit on the azimuth positioner with the probe axis perpendicular to the FSS. The forward scattered field is measured by rotating the azimuth positioner through an angle θ . The phased array model is no longer valid because at each incident angle θ , the amplitude and phase response of the FSS is different. Also, since the receive probe has been moved up to $d = .114$ m away from the FSS, the receive probe and FSS aperture patterns need to be included in the calculations. The LPT method takes into account the receive probe and aperture patterns and is the technique studied for the remainder of the chapter. The FSS was reduced in size by masking the surface with conducting tape so it was 17 apertures wide in the x -direction and 8 apertures wide in the y -direction. The scattered field

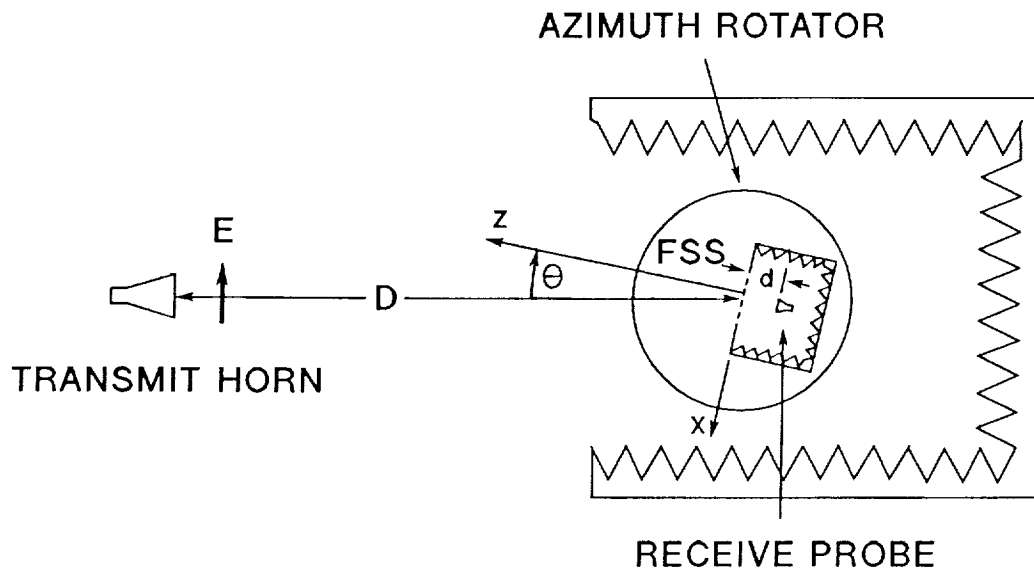


Figure 5.7. Experimental configuration for measuring the scattered field from the FSS with the incident plane wave sweeping through an angle θ . Note the FSS and receive probe both rotate on the azimuth positioner. The FSS orientation is given in Fig. 2.1.

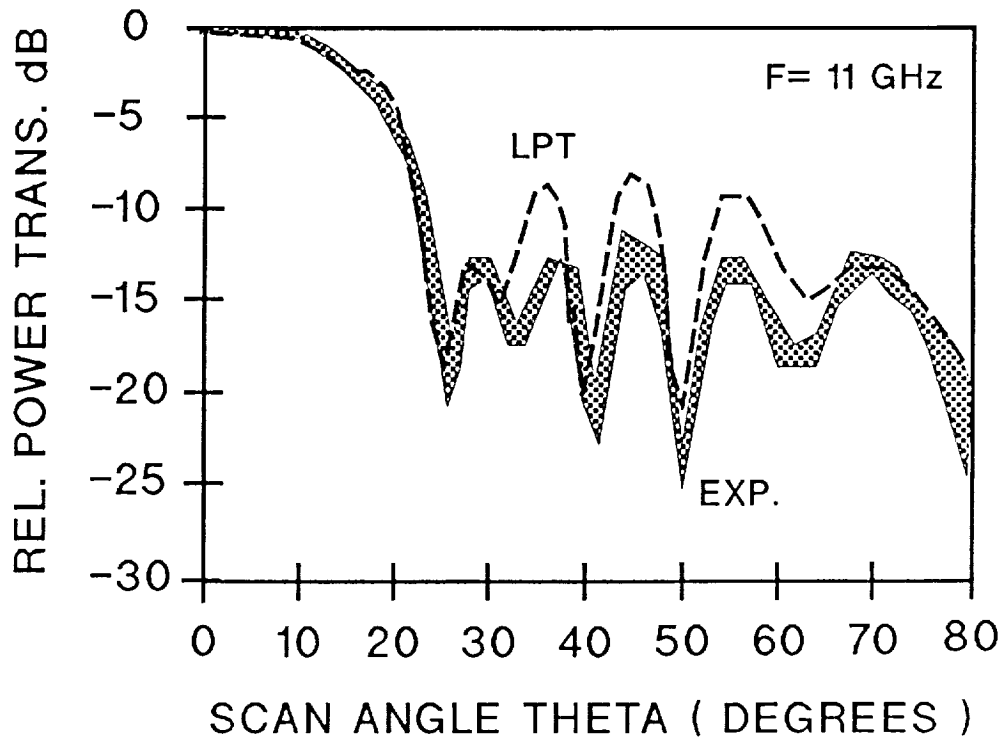


Figure 5.8. Forward scattered field as a function of incident angle θ for a FSS with 17 apertures in the x -direction and 8 apertures in the y -direction. The operating frequency is 11 GHz. The test setup is shown in Fig. 5.7 with $D = 15$ m and $d = .114$ m. The FSS dimensions are found in Fig. 4.1 and the incident electric field is E_x .

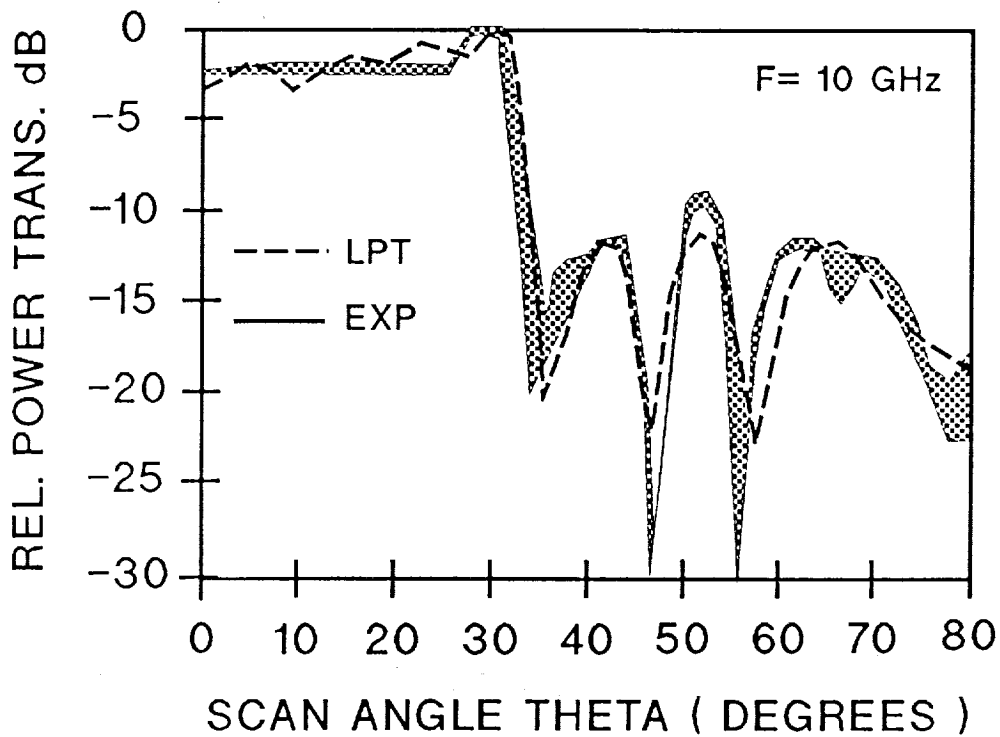


Figure 5.9. Forward scattered field as a function of incident angle θ for a FSS with 17 apertures in the x -direction and 8 apertures in the y -direction. The operating frequency has been changed to 10 GHz. The test setup is shown in Fig. 5.7 with $D = 15$ m and $d = .114$ m. The FSS dimensions are found in Fig. 4.1 and the incident electric field is E_x .

pattern measured at 11 GHz is shown by the shaded area in Fig. 5.8. The two lines bounding the shaded region are data from the positive and negative θ scans. By shading in the difference between the two curves, the non-symmetry of the experimental data is revealed. The LPT calculation is shown by the dashed line. To check the behavior of the theory with respect to frequency, the experiment was repeated at 10 GHz. Figure 5.9 shows the experimental and LPT results. Note how the main lobes have flattened and there is a transmission peak at $\theta = 30^\circ$. This peak corresponds to the transmission maximum found in the infinite FSS study illustrated in Fig. 4.5 for an incidence angle of 30° .

The experiments in this section have explored the scattered field from the planar FSS illuminated by a plane wave. The results in this section were quite good because the incident wavefront was nearly planar and the surface was flat. However, the LPT can address non-planar incidence as well as curved FSSs. In the next two sections, the capabilities and limitations of the LPT will be studied in terms of incident wavefront and FSS curvature.

5.3. Study of the LPT Accuracy as a Function of Incident Field Curvature

The LPT assumes the incident field can be approximated by a number of plane waves incident on different regions of the FSS. An important question is how does the accuracy of the forward scattered field depend on the incident field wavefront? As the incident plane wave becomes non-planar, the infinite FSS theory invoked at each subarray becomes a progressively poorer approximation to the actual surface response. In this section the limitations of the LPT accuracy due to non-planar illumination will be studied by an experimental and numerical investigation of the forward scattered fields from a planar FSS with spherical wave illumination. The experimental and LPT results will be compared as the distance between the feed source and FSS is reduced until a

degradation in the numerical analysis is observed.

Figure 5.10 illustrates the experimental setup for the study. The FSS was masked off to be 11×8 apertures wide in the x and y -directions, respectively. The receive probe was positioned at $d = .8$ m from the FSS. The choice of receive probe distance was arbitrary. However, there are two reasons for choosing a large value of d . The first reason is to reduce the standing wave effect discussed in Chapter 4 for the angles around $\theta = 0^\circ$. The second reason is the nulls in the experimental scattered field pattern fill as the receive probe is moved closer to the FSS. Thus, the larger d value provides a better resolution of the scattered field pattern nulls. This makes it easier to compare theory and experiment. The experiment was performed in a large laboratory room with absorber blocks placed around the experiment. Figure 5.11 is a photograph of the feed source. The feed was a pyramidal horn placed in an absorber enclosure. Figure 5.12 shows a view taken from behind the feed horn looking at the FSS placed in the absorber wall. The feed was mounted on a tripod and was moved to various locations to investigate the effect of different spherical wavefront curvatures on the experimental and LPT response. The masking of the apertures shown in the photo is different from the actual masking used in the experiment. Figure 5.13 is a view of the scattered field area of the experiment. The receive probe consisted of an open ended circular waveguide with a ground plane choke ring surrounded by absorber. While not obvious from the photo, the rotating positioner's center of rotation is directly below the FSS. Also visible on the absorber wall is a pair of wooden forms used to bend the FSS into a hyperbolic cylinder for non-planar testing.

The experiment began by placing the feed at a distance $D = .76$ m. Figure 5.14 shows the experimental and LPT results for $D = .76$ m. The sidelobe peaks and nulls are well predicted for this feed to FSS distance. The feed was moved in to $D = .46$ m and the experiment was repeated. The results, given in

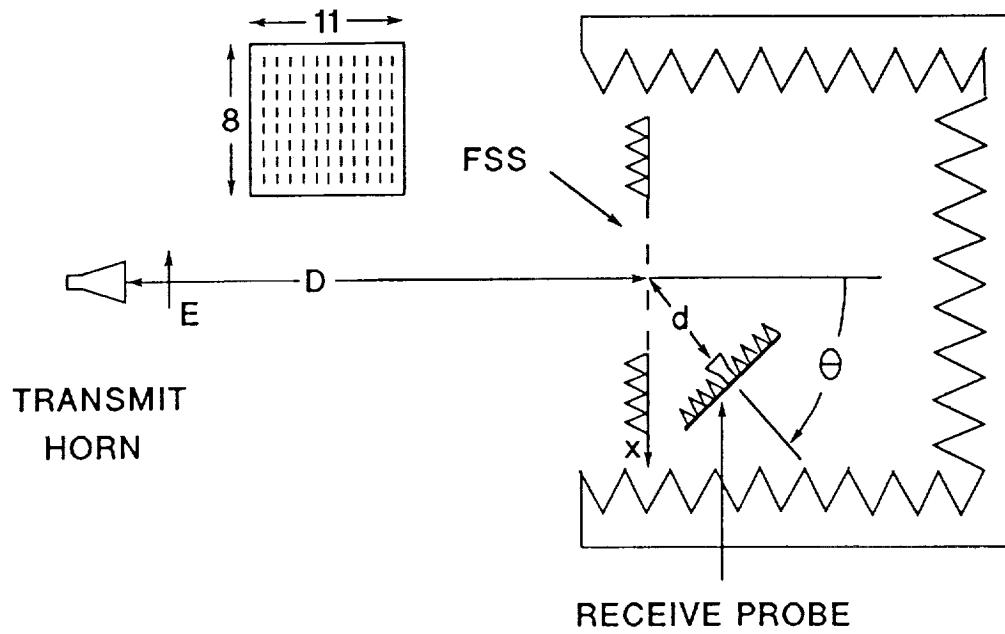


Figure 5.10. Experimental configuration for measuring the scattered field from the FSS to determine the limitations of the LPT in terms of incident field curvature. The distance D will be varied in the experiment. The receive probe distance remains fixed at $d = .8$ m.

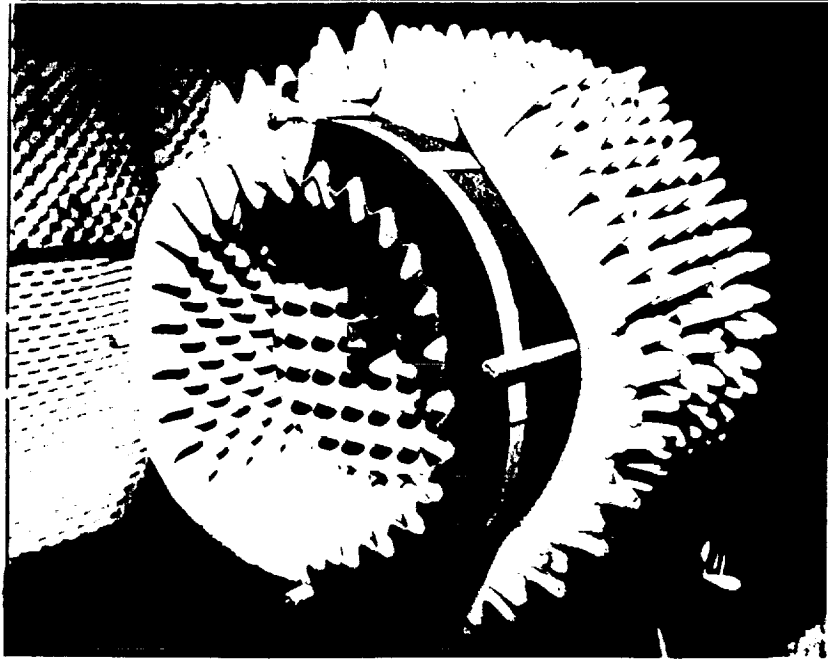


Figure 5.11. Photograph of the pyramidal horn transmit antenna. This setup was also the receive probe and FSS support for the experiment illustrated in Fig. 5.7.

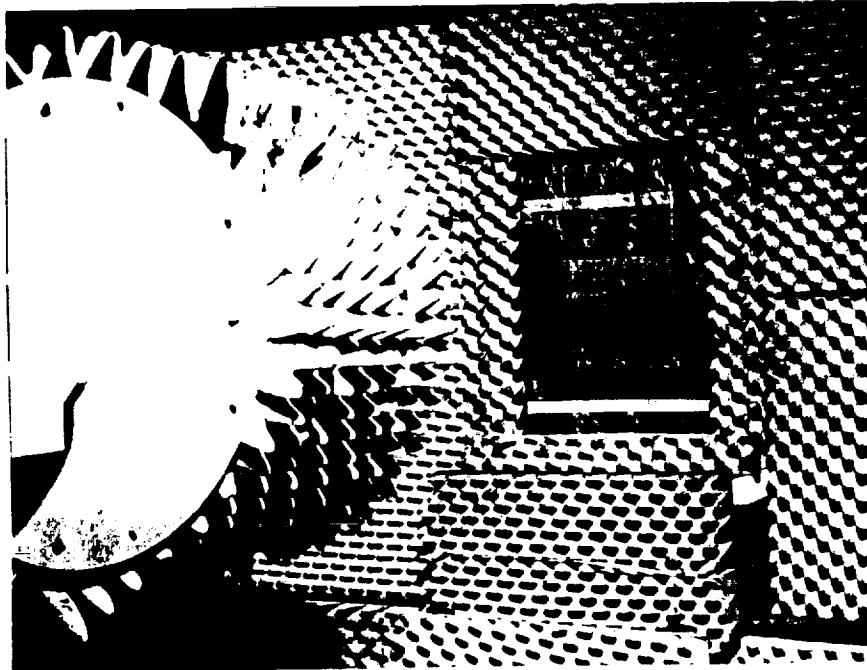


Figure 5.12. Photograph of experiment looking from the rear of the transmit horn to the FSS positioned in the absorber wall. When the photo was taken the FSS was masked for the hyperbolic cylinder tests presented in the next section.

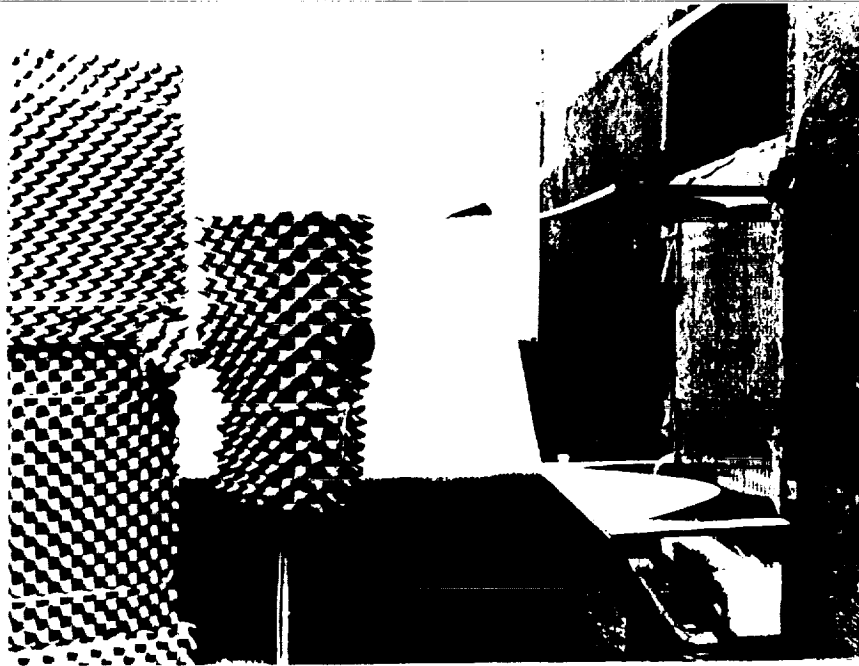


Figure 5.13. Photograph of the forward scattered field region showing the receive probe on the rotating arm. The positioner's center of rotation is located directly below the center of the FSS. Also visible is a wooden template used to form the hyperbolic cylinder FSS geometry discussed in the next section.

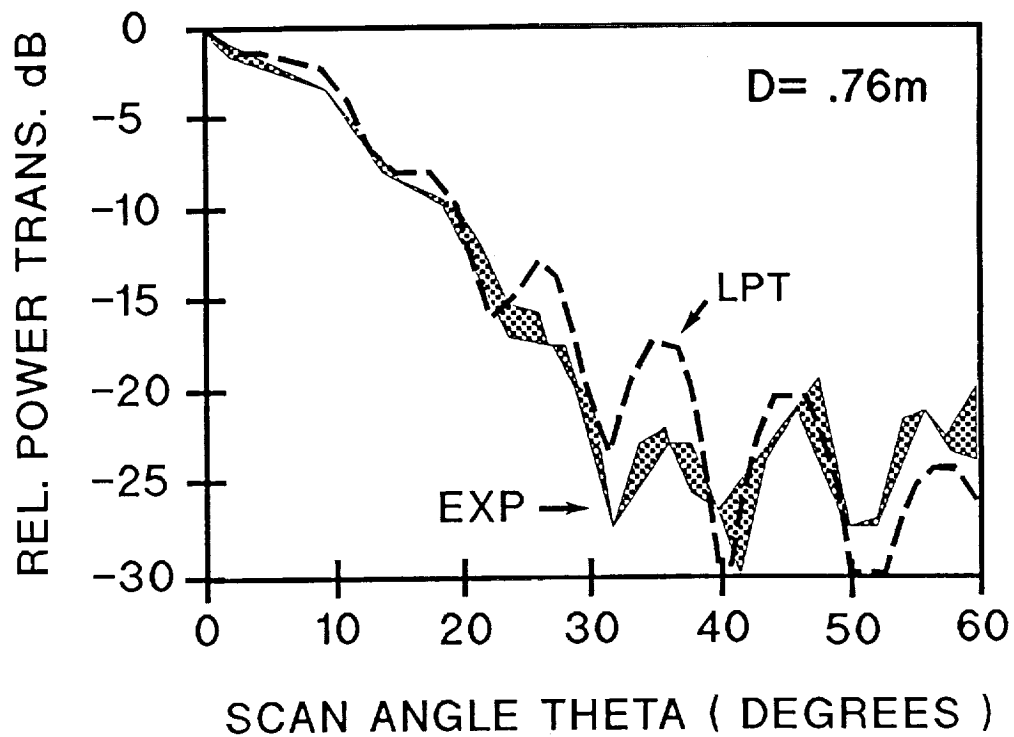


Figure 5.14. Scattered field experimental result for the configuration given in Fig. 5.10. The transmit horn is located at $D = .76\text{m}$. The incident electric field is polarized along the x -axis and the frequency is 11 GHz. The FSS dimensions are found in Fig. 4.1.

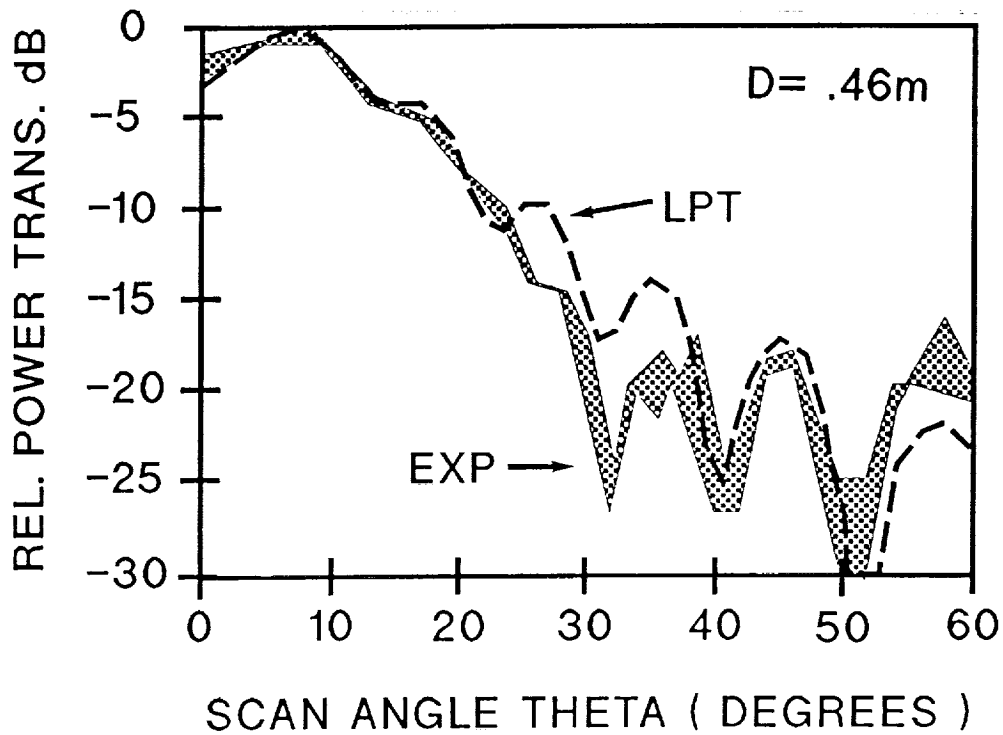


Figure 5.15. Forward scattered field for $D = .46$ m. At this distance, the LPT provides satisfactory prediction of the experimental sidelobe peaks and nulls. The incident electric field is polarized along the x -axis and the frequency is 11 GHz. The FSS dimensions are found in Fig. 4.1.

Fig. 5.15, show the main lobe and sidelobe structure are still well predicted. However, the LPT null at the 30° scan angle is filling. Note at this illumination distance the transmission response from $0 - 25^\circ$ is predicted remarkably well. This distance represents the closest the feed could come to the FSS and still retain good agreement between the LPT and experiment. Figures 5.16 and 5.17 show the scattered field results for $D = .3$ m and $D = .13$ m, respectively. At $D = .3$ m the experimental null at 30° is no longer predicted and at $D = .13$ m, the LPT calculation degrades even further. The failure of the LPT is a gradual process and the determination of the distance D is dependent on the degree of accuracy desired.

The loss of accuracy in the LPT is due to the difference in the spherical wavefront's phase distribution over the FSS as compared to the phase of a plane wave. To visualize the phase error between the plane and spherical wavefronts, consider Fig. 5.18. The transmit horn is positioned at a distance D from the FSS represented as the horizontal line. A unit cell of the FSS is given by the dimension W . The dotted line P represents the wavefront from a plane wave incident on the FSS center. Due to the proximity of the feed, there is phase error ξ in degrees between the center of the unit cell and the edge given by the expression

$$\xi = 360 \frac{(L - D)}{\lambda}, \quad (5.1)$$

where λ is the resonant wavelength for the FSS. Also shown in the figure is the case of non-normal incidence upon the FSS, illustrated by the subscripted variables. By considering the geometry, one can find the phase difference between the center and edge of the off-axis unit cell is always less than the phase difference for the on-axis case. Figure 5.19 is a graph of the phase error between a spherical and plane wave illumination for the experimental unit cell. The thin vertical lines represent the distances at which each experiment was

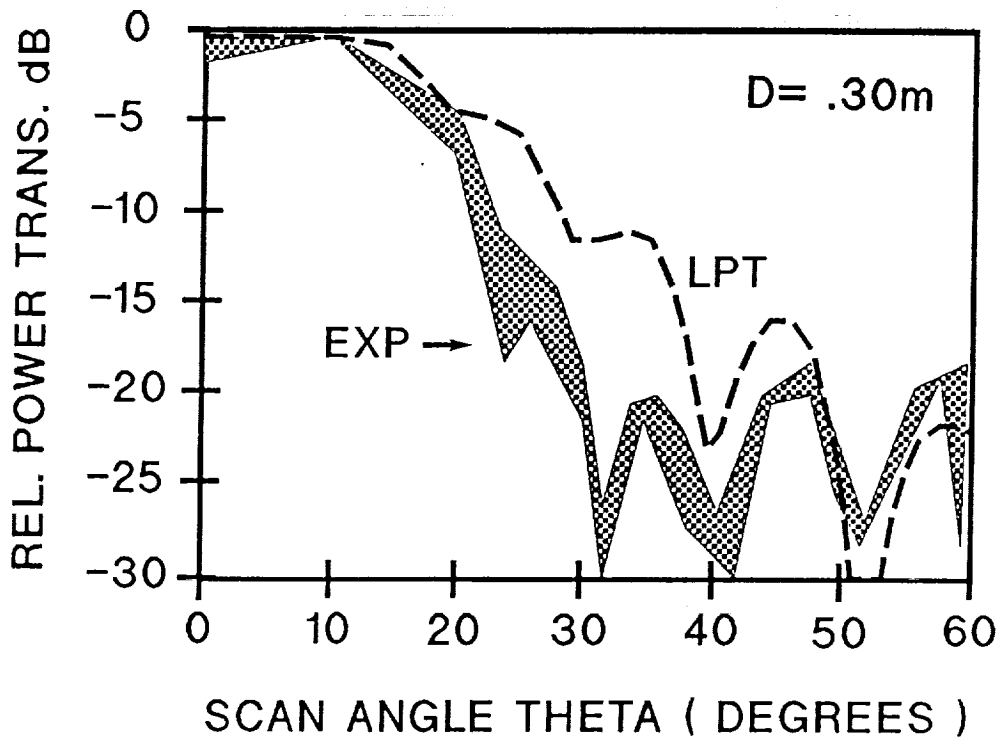


Figure 5.16. Forward scattered field for $D = .3$ m. The 30° experimental null is no longer predicted by the LPT. The incident electric field is polarized along the x -axis and the frequency is 11 GHz. The FSS dimensions are found in Fig. 4.1.

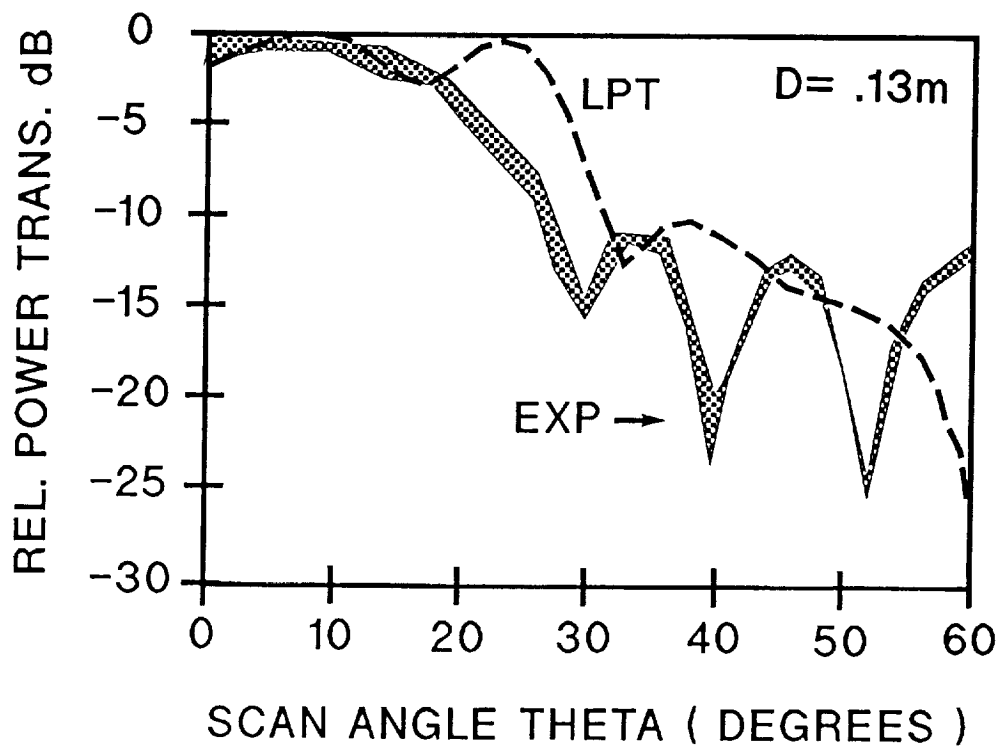


Figure 5.17. Forward scattered field for $D = .13m$. Only the first 20° of the pattern is predicted. The incident electric field is polarized along the x -axis and the frequency is 11 GHz. The FSS dimensions are found in Fig. 4.1.

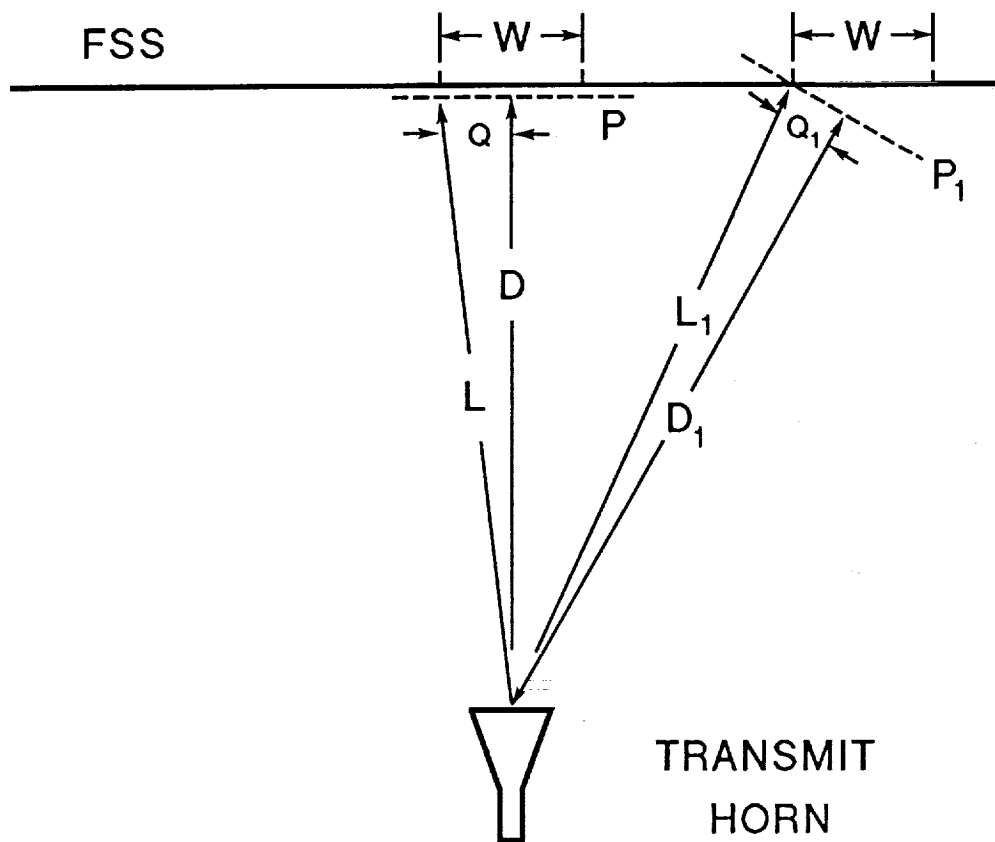


Figure 5.18. Diagram for calculating the phase error over a unit cell due to a spherical source located a distance D from the FSS.

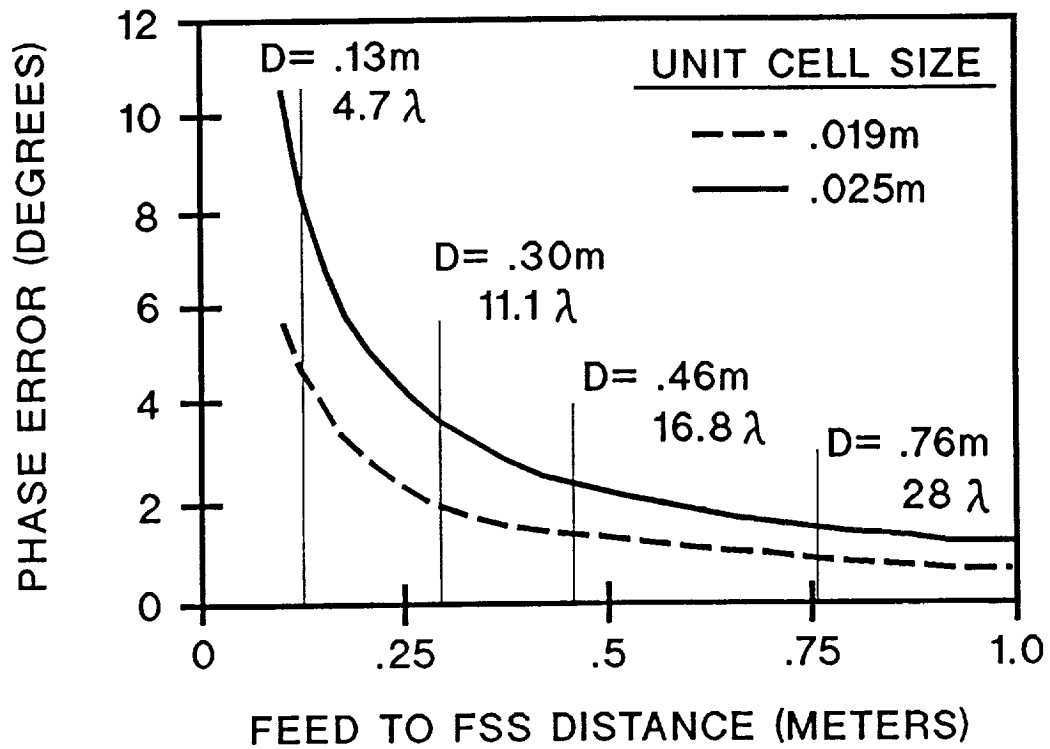


Figure 5.19. Phase error over a unit cell due to spherical wave illumination at a distance D from the FSS. The solid and dashed curves represent the y and x -direction unit cell dimensions, respectively. The resonant wavelength is λ .

performed. Also shown for each distance is the equivalent distance measured in resonant wavelengths λ . From the experimental and numerical results, the region where the LPT theory is no longer valid occurs at around $D = .46$ m. At closer distances, the phase error rises rapidly resulting in the LPT and experimental scattered field differences. So, for the experimental planar FSS, the LPT and experimental results are in good agreement until a phase error over a unit cell of about 2° or 3° occurs.

5.4. Study of the LPT Accuracy as a Function of Surface Curvature

The LPT accuracy is expected to deteriorate with increasing curvature since the infinite planar solution for each subarray becomes less accurate. The limitation of the LPT due to surface curvature was studied by considering the forward scattered field from a set of hyperbolic cylinders of varying curvature. The hyperbolic cylinders, illustrated in Fig. 5.20, are independent of y . The equation for the hyperbola in the x, z plane, for z as a function of x , is

$$z = h_a \left(1 - \sqrt{1 + \left(\frac{x}{h_b} \right)^2} \right). \quad (5.2)$$

Several hyperbolic cylinders identified by the notation H0-H3 were studied. The hyperbolic parameters h_a and h_b for each curve are given in Table 5.1. The hyperbolas were formed by taping the FSS to a wooden form as was seen in Fig. 5.12. The FSS was masked off to be 29×8 apertures in the x and y -directions, respectively. Figure 5.20 also illustrates the hyperbolic cylinder experimental configuration. The transmit feed horn was positioned at a distance $D = 1.75$ m to avoid any non-planar wave illumination problems. The receive probe distance of $d = .8$ m remained the same as in the previous experiment.

The first hyperbolic cylinder forward scattered field experiment was for the case of zero curvature. The experimental and computed scattered field results are shown in Fig. 5.21. As expected, the theory and experiment are in

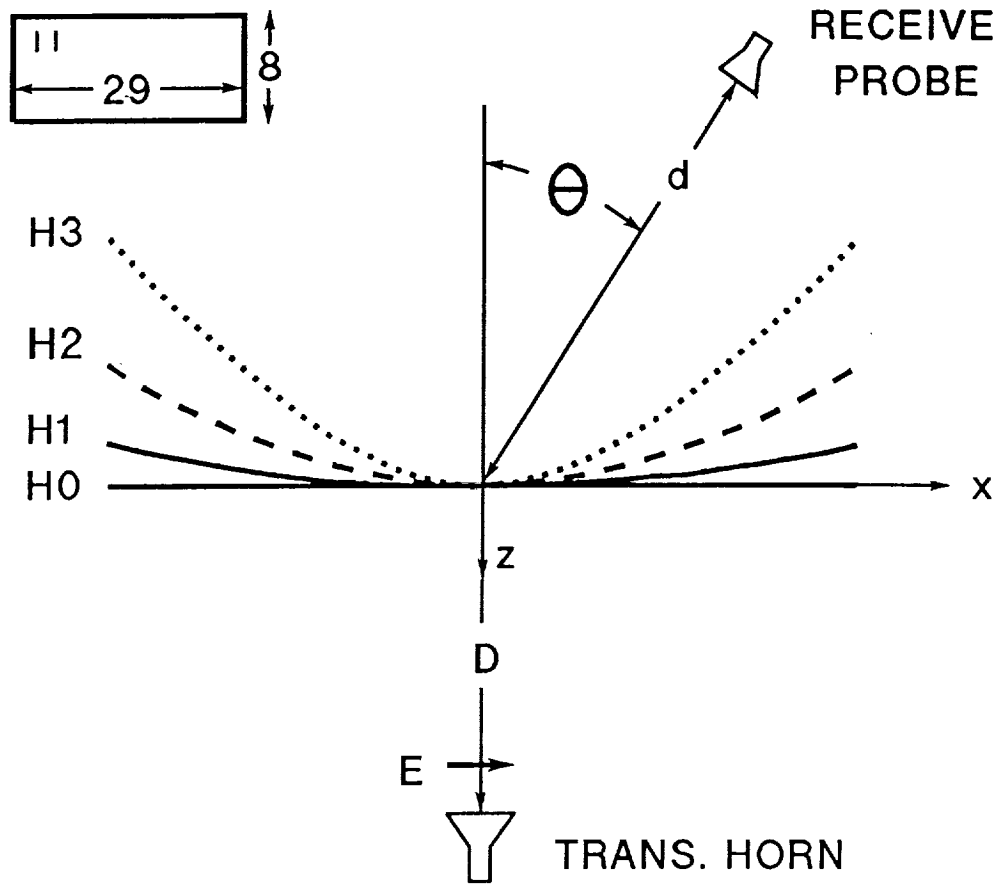


Figure 5.20. Hyperbolic cylinder FSS geometry. H0-H3 represent the different FSS curvatures studied. The hyperbolic cylinder is extended parallel to the y -axis. The hyperbolic parameters are given in Table 5.1. The FSS orientation is given by the x -axis.

Curve	h_a	h_b
H0	0	—
H1	.217	.508
H2	.217	.281
H3	.217	.178

Table 5.1. Table of hyperbola parameters for the different hyperbolic cylinders studied. The parameter dimensions are in meters.

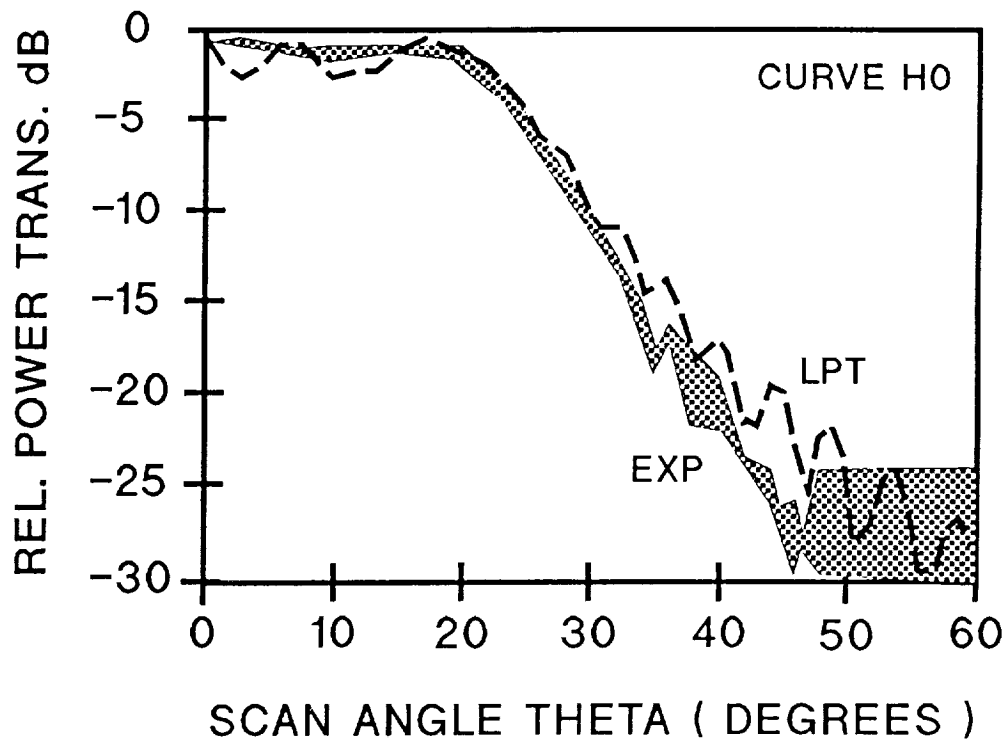


Figure 5.21. Forward scattered field from the hyperbolic cylinder H0. The FSS is flat in this case. The incident electric field is polarized along the x -axis and the frequency is 11 GHz. The FSS dimensions are found in Fig. 4.1.

good agreement. Figure 5.22 is the result for hyperbolic cylinder H1. The main lobe was well predicted; however, the sidelobes beyond 30° are not predicted by the LPT. The large shaded region is due to the rapid oscillation of the sidelobe structure. Figure 5.23 is the case for hyperbolic cylinder H2. The main beam is well predicted and the first sidelobe is predicted in position but the LPT exhibits a large error in magnitude. Once again after about 30° the measured sidelobes are greater than the LPT calculated values. Finally, Fig. 5.24 shows the results from hyperbolic cylinder H3. The curvature in this case is becoming large and thus there should be no surprise that indeed the theory and experiment differ. Note that even at this curvature, the main beam and first null are predicted quite well.

The hyperbolic cylinder results do not show the gradual decrease in accuracy as was seen in the non-planar illumination study. Rather, the response out to 30° , or the mainbeam in the case of H3, remained good for all curvatures studied. At scans greater than about 30° , the LPT was poor in predicting the experimental response.

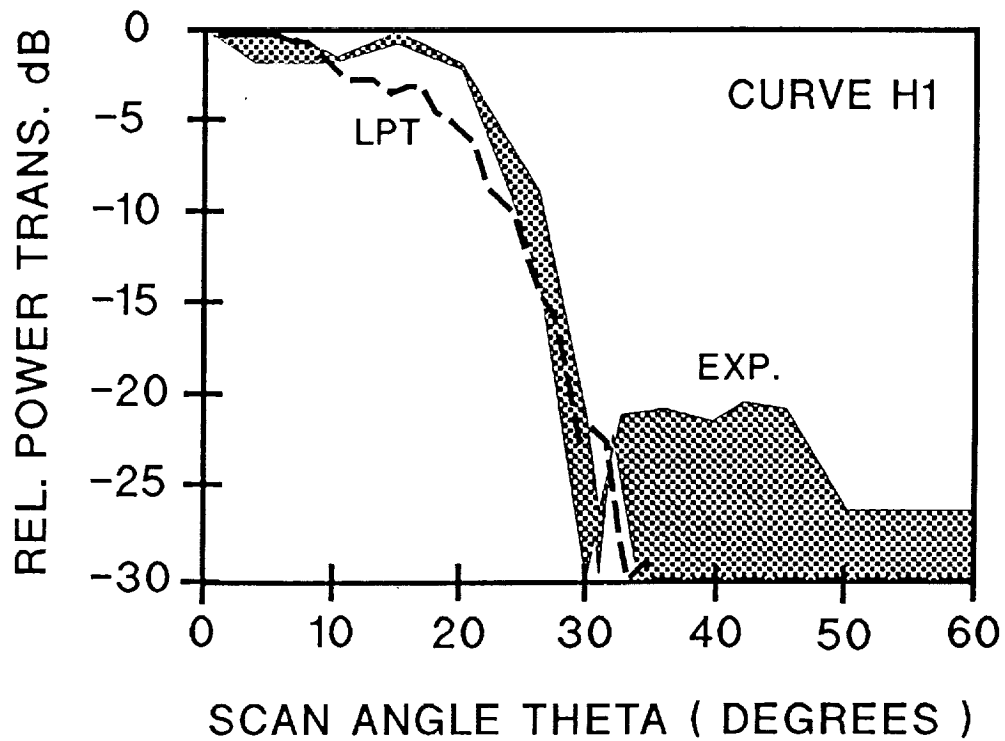


Figure 5.22. Forward scattered field from the hyperbolic cylinder H1. The LPT and experiment are in good agreement out to 30° after which the LPT result falls below the oscillating experimental results. The incident electric field is polarized along the x -axis and the frequency is 11 GHz. The FSS dimensions are found in Fig. 4.1.

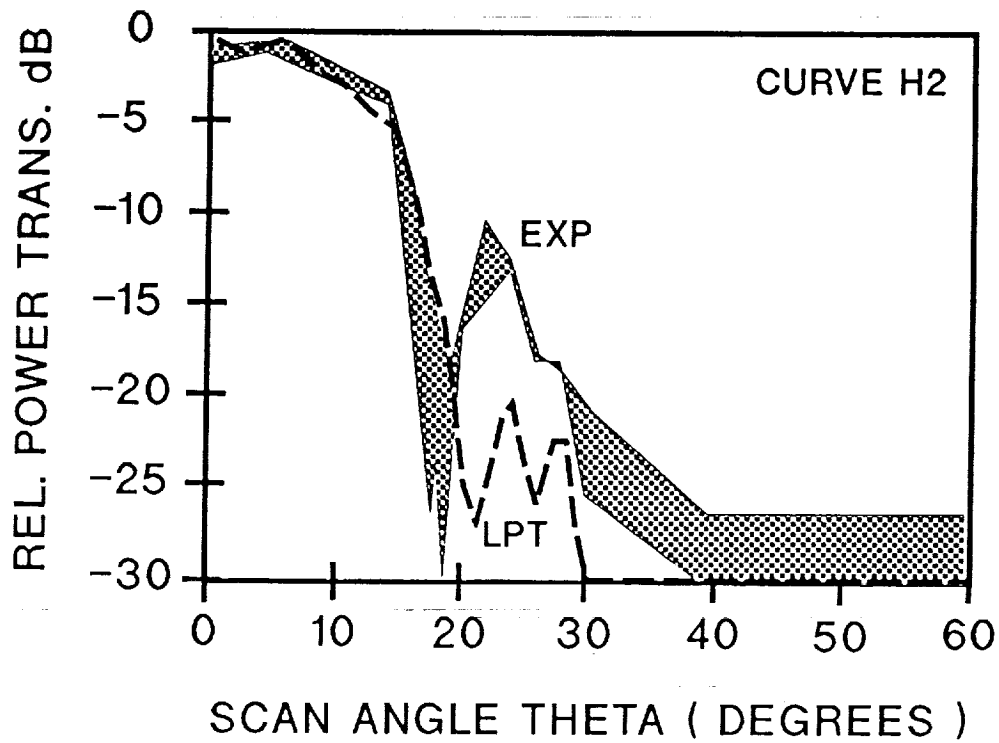


Figure 5.23. Forward scattered field from the hyperbolic cylinder H2. The main lobe is predicted well however the experimental sidelobe level is higher than the LPT calculation. The incident electric field is polarized along the x -axis and the frequency is 11 GHz. The FSS dimensions are found in Fig. 4.1.

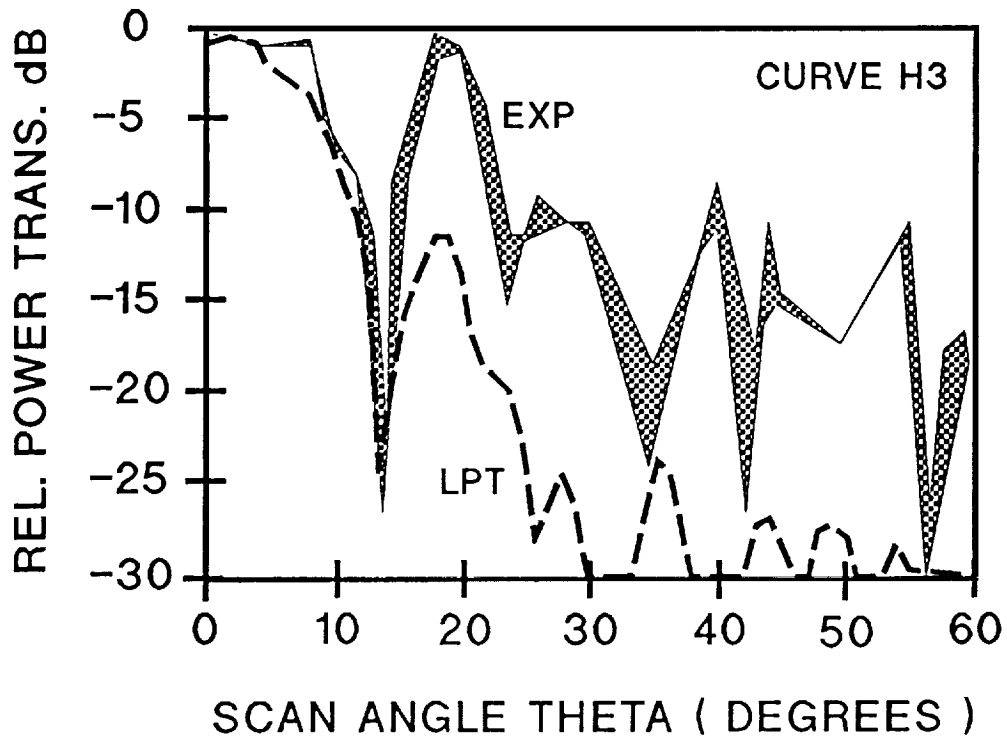


Figure 5.24. Forward scattered field from the hyperbolic cylinder H3. The main lobe and first sidelobe are predicted well. However the large curvature in this case is causing problems with the accuracy of both theory and experiment. The incident electric field is polarized along the x -axis and the frequency is 11 GHz. The FSS dimensions are found in Fig. 4.1.

CHAPTER 6

CONCLUSIONS

As a result of the experimental FSS study, the infinite FSS numerical solution has been verified for both the amplitude and phase of the transmission coefficient. The results show both full domain and subsectional rooftop basis functions can accurately predict the frequency response of the FSS. No evidence was found to support the use of a relative convergence criterion.

The forward scattered field experiments revealed for a single plane wave incidence on the planar FSS that the transmitted field can be approximated by the array factor. If the angle of incidence changes during the scan of the planar FSS, the forward scattered field is well predicted by the LPT. The limitation of the LPT in terms of incident wavefront and FSS surface curvature was determined by comparisons of theory with experimental results. For the planar FSS, with spherical wave illumination, the maximum difference in phase between the center and edge of the unit cell for good agreement between the LPT model and experimental results was found to be about 2 or 3 degrees. The experiments to determine the effect of surface curvature on the LPT accuracy did not show a simple degradation in accuracy as the surface was changed to different hyperbolic curvatures. Rather, for all the hyperbolic cylinders studied, the LPT predicted the response accurately near the main beam followed by large errors in the sidelobes beyond 30° .

The results from the FSS study can be applied to determine if the LPT can be used in the design of a specific FSS systems. If the FSS aperture geometry is much different than the experimental FSS used in the experiments, the LPT experiments discussed would need to be repeated to determine the appropriate guidelines for the particular surface.

REFERENCES

- [1] T. Cwik, R. Mittra, K.C. Lang, and T.K. Wu, "Frequency selective screens," *IEEE Antennas Propagat. Newsletter*, Apr. 1987, pp. 6-10.
- [2] C.A. Balanis, *Antenna Theory*. New York: Harper and Row, 1982, pp. 496-501.
- [3] V.D. Agrawal and W.A. Imbriale "Design of a dichroic cassegrain subreflector," *IEEE Trans. Antennas Propagat.*, vol. AP-27, no. 4, July 1979, pp. 466-473.
- [4] W. L. Ko, and R. Mittra, "Scattering from an array of metallic patches located on a curved surface." *IEEE AP-S Symposium Digest*, Syracuse, NY, 1988, pp. 642-645.
- [5] R.H. Ott, R.G. Kouyoumjian, and L. Peters, Jr., "Scattering by a two dimensional periodic array of narrow plates," *Radio Science*, vol. 2, Nov. 1967, pp. 1347-1359.
- [6] C.C. Chen, "Scattering through a conducting screen perforated periodically with apertures," *Microwave theory and techniques*, vol. MTT-18, Sep. 1970, pp. 627-632.
- [7] J.A. Arnaud and F.A. Pelow, "Resonant-grid quasi-optical diplexers," *The Bell System Technical Journal*, vol. 54, no. 2, Feb. 1975, pp. 263-283.
- [8] C.H. Tsao, R. Mittra, "Spectral domain analysis of frequency selective surfaces comprised of periodic arrays of crossed dipoles and jerusalem crosses," *IEEE Trans. Antennas Propagat.*, vol. AP-32, May 1984, pp. 478-486.
- [9] C. Scott, *The Spectral Domain Method in Electromagnetics*. Boston: Artech House, 1989.
- [10] R.F. Harrington, *Time Harmonic Electromagnetic Fields*. New York: McGraw-Hill Book Co., 1961, p. 108.
- [11] N. Amitay, V. Galindo, and C. P. Wu, *Theory and Analysis of Phased*

- Array Antennas*. New York: Wiley-Interscience, 1972, pp. 37-40.
- [12] C. Scott, *o.p. cit*, ref. 9, pp. 127-12.
 - [13] R. F. Harrington, *Field Computation by Moment Methods*. New York: Macmillan Co., 1968, p. 7.
 - [14] R. Mittra, C.H. Chan, and T. Cwik, "Techniques for analyzing frequency selective surfaces - a review," *Proceedings of the IEEE*, vol. 76, no. 12, Dec. 1988, pp. 1593-1615.
 - [15] G.A. Korn and T.M. Korn, *Mathematical Handbook for Scientists and Engineers*, New York: McGraw-Hill Book Co., 1961, p. 724.
 - [16] Caltech, *Tables of Integral Transforms - Manuscript Project*, vol. 1, New York: McGraw-Hill Book Co., 1954, p. 368.
 - [17] D.N. Green and S.C. Bass, "Signal representation with triangular basis functions," *Electronic Circuits and Systems*, vol. 3, no. 2, Mar. 1979, pp. 58-68.
 - [18] B.J. Rubin, and H. L. Bertoni, "Reflection from a periodically perforated plane using a subsectional current approximation," *IEEE Trans. Antennas Propagat.*, vol. AP-31, Nov. 1983, pp. 829-836.
 - [19] R. Bracewell, *The Fourier Transform and Its Applications* New York: McGraw-Hill Book Co., 1965, p. 244.
 - [20] C.H. Tsao, and R. Mittra "A spectral-iteration approach for analyzing scattering from frequency selective surfaces," *IEEE Trans. Antennas Propagat.*, vol. AP-30, no. 2, Mar. 1982, pp. 303-308.
 - [21] N.G. Alexopoulos, P.L.E. Uslenghi, and N.K. Uzunoglu, "Microstrip dipoles on cylindrical structures," *Proc. Antenna Applications Symp.*, Univ. of Illinois, Sep. 1981. pp. 1-20.
 - [22] R. Mittra, and T. Cwik, "The effects of the truncation and curvature of periodic surfaces: a strip grating," *IEEE Trans. Antennas Propagat.*, vol. 36, no. 5, May 1988, pp. 612-622.

- [23] R.E. Collin, *Antennas and Radiowave Propagation*. New York: McGraw-Hill Book Co., 1985, p. 169.
- [24] N.V. Shuley, "Measurements on dichroic surfaces," Technical report no. 8409, Division of Network Theory, Chalmers University of Technology, Göteborg, Sweden, Dec. 1984.
- [25] T. Cwik, R. Mittra, H.H. Ohta, and K.C. Lang, "Numerical convergence and accuracy studies for the prediction of null frequencies of the jerusalem cross frequency selective surface," *IEEE APS-URSI Symp. Digest*, 1984, pp. 921-924.
- [26] K.J. Webb, A. Caroglanian, P.W. Grounds, and R. Mittra, "Numerical convergence in dichroic problems." *Microwave and Optical Technology Letters*, vol. 1, no. 9, Nov. 1988, pp. 317-320.
- [27] C.H. Tsao, and R. Mittra, "Spectral-domain analysis of frequency selective surfaces comprised of periodic arrays of cross dipoles and jerusalem crosses," *IEEE Trans. Antennas Propagat.*, vol. AP-32, no. 5 May 1984, pp. 478-486.
- [28] R. Mittra, R.C. Hall, and C.H. Tsao "Spectral-domain analysis of circular patch frequency selective surfaces," *IEEE Trans. Antennas Propagat.*, vol. AP-32, no. 5 May 1984, pp. 533-536.
- [29] F.S. Johansson, "Analysis and design of double-layer frequency-selective surfaces," *IEE Proceedings*, vol. 132, pt. H, no. 5, Aug. 1985, pp. 319-325.
- [30] N.V. Shuley, "Higher-order mode interaction in planar periodic structures," *IEE Proceedings*, vol. 131, Pt. H, no. 3, June 1984, pp. 129-132.
- [31] A. Caroglanian, P. W. Grounds, and K.J. Webb, "Finite and infinite frequency selective surfaces: experiments and models." Accepted for publication in *The Journal of Electromagnetic Waves and Applications*, 1989.



Report Documentation Page

1. Report No. NASA TM-104540		2. Government Accession No.		3. Recipient's Catalog No.	
4. Title and Subtitle Numerical and Experimental Study of Curved and Planar Frequency Selective Surfaces with Arbitrary Illumination			5. Report Date April 1991		
			6. Performing Organization Code 531.2		
7. Author(s) Armen Caroglanian			8. Performing Organization Report No. 91E01722		
			10. Work Unit No.		
9. Performing Organization Name and Address RF System Section Goddard Space Flight Center Greenbelt, Maryland 20771			11. Contract or Grant No.		
			13. Type of Report and Period Covered Technical Memorandum		
12. Sponsoring Agency Name and Address National Aeronautics and Space Administration Washington, D.C. 20546-0001			14. Sponsoring Agency Code		
			15. Supplementary Notes <p>This report is a thesis submitted to the Faculty of the Graduate School of the University of Maryland in partial fulfillment of the requirements for the degree of Master of Science, 1989.</p>		
16. Abstract A frequency selective surface (FSS) composed of apertures in a metallic sheet is known as an inductive FSS. The infinite inductive FSS theory is derived and the aperture fields are solved by a spectral domain formulation with method of moments solution. Both full domain and subsectional basis functions are studied. A locally planar technique (LPT) is used to determine the forward scattered field from a generally shaped inductive FSS with arbitrary illumination. An experimental FSS study is presented to verify both the infinite FSS theory and to determine the accuracy of the LPT. The infinite planar FSS transmission coefficient measured as a function of frequency is compared with theory. The inductive FSS's forward scattered field is experimentally measured and compared to the LPT. A series of experiments with the spherical feed source at varying distances from the planar FSS is used to determine the limitations of the LPT in terms of the incident phase error over a unit cell. The limitations of the LPT because of surface curvature are investigated by an experimental study of the scattered fields from a set of hyperbolic cylinders of different curvatures. From the experiments, guidelines for applying the LPT are developed.					
17. Key Words (Suggested by Author(s)) frequency selective surfaces, dichroic, scattering, microwave, numerical methods			18. Distribution Statement Unclassified - Unlimited Subject Category 33		
19. Security Classif. (of this report) Unclassified		20. Security Classif. (of this page) Unclassified		21. No. of pages 92	22. Price

END DATE JAN 7, 1992